

# Realistic modelling of wind and supernovae shocks in star clusters: addressing $^{22}\text{Ne}/^{20}\text{Ne}$ and other problems in Galactic cosmic rays

Siddhartha Gupta,<sup>1,2,3</sup> Biman B. Nath,<sup>1★</sup> Prateek Sharma<sup>2,4</sup> and David Eichler<sup>5</sup>

<sup>1</sup>Raman Research Institute, Sadashiva Nagar, Bangalore 560080, India

<sup>2</sup>Department of Physics, Indian Institute of Science, Bangalore 560012, India

<sup>3</sup>Department of Astronomy and Astrophysics, University of Chicago, IL 60637, USA

<sup>4</sup>MPI für Astrophysik, Karl-Schwarzschild str 1, D-85741 Garching, Germany

<sup>5</sup>Department of Physics, Ben-Gurion University, Beer Sheva, Israel

Accepted 2020 January 21. Received 2020 January 6; in original form 2019 October 18

## ABSTRACT

Cosmic ray (CR) sources leave signatures in the isotopic abundances of CRs. Current models of Galactic CRs that consider supernovae (SNe) shocks as the main sites of particle acceleration cannot satisfactorily explain the higher  $^{22}\text{Ne}/^{20}\text{Ne}$  ratio in CRs compared to the interstellar medium. Although stellar winds from massive stars have been invoked, their contribution relative to SNe ejecta has been taken as a free parameter. Here, we present a theoretical calculation of the relative contributions of wind termination shocks (WTSs) and SNe shocks in superbubbles, based on the hydrodynamics of winds in clusters, the standard stellar mass function, and stellar evolution theory. We find that the contribution of WTSs towards the total CR production is at least 25 per cent, which rises to  $\gtrsim 50$  per cent for young ( $\lesssim 10$  Myr) clusters, and explains the observed  $^{22}\text{Ne}/^{20}\text{Ne}$  ratio. We argue that since the progenitors of apparently isolated supernovae remnants (SNRs) are born in massive star clusters, both WTS and SNe shocks can be integrated into a combined scenario of CRs being accelerated in massive clusters. This scenario is consistent with the observed ratio of SNRs to  $\gamma$ -ray bright ( $L_\gamma \gtrsim 10^{35}$  erg s $^{-1}$ ) star clusters, as predicted by star cluster mass function. Moreover, WTSs can accelerate CRs to PeV energies, and solve other long-standing problems of the standard SN paradigm of CR acceleration.

**Key words:** hydrodynamics – shock waves – methods:numerical – cosmic rays.

## 1 INTRODUCTION

Cosmic rays (CRs) have been thought to be mostly accelerated by supernovae (SNe) through shocks running into the interstellar medium (ISM, Grenier, Black & Strong 2015). One of the main arguments for this is the energy requirement of Galactic CRs (GCRs) to maintain a steady CR luminosity. This scenario demands  $2 \pm 1$  SNe explosions per century in our Galaxy, given that  $\sim 10$  per cent of SNe energy goes to CRs (Diehl et al. 2006). However, this standard scenario is known to bear several ailing problems (e.g. Gabici et al. 2019) and additional/complementary sources of CRs have been sought in the literature. One such problem concerns the abundance ratios of certain isotopes which are different from solar abundances and yet not secondary products (e.g. Mewaldt 1981). For example, the observed ratio of  $^{22}\text{Ne}$  to  $^{20}\text{Ne}$  in GCRs is  $5.3 \pm 0.3$  times the solar value (Wiedenbeck & Greiner 1981; Maeder & Meynet 1993; Binns et al. 2008), and it cannot be satisfactorily explained by SNe shocks in the ISM.

It has been suggested that this observed anomalous ratio in GCRs can be explained if SN shocks in superbubbles (SBs) played a major role in accelerating CRs because the gas inside an SB is rich in  $^{22}\text{Ne}$ , ejected in the winds of massive stars (Higdon & Lingenfelter 2003; Binns et al. 2008). This fits in with the mounting evidence of CRs being accelerated in star clusters, as predicted by Cesarsky & Montmerle (1983). A signature of CRs in the form of  $\gamma$ -radiation has been detected in massive star clusters such as Cyg OB2, which are too young ( $\lesssim 3$  Myr) to have had SN (Ackermann et al. 2011). Moreover,  $\gamma$ -ray luminosities of these clusters is  $\sim 0.1$  per cent of the wind mechanical power ( $L_w$ ) feeding the cluster (Ackermann et al. 2011; Yang, de Oña Wilhelmi & Aharonian 2018), and therefore it raises the possibility of a significant contribution from young star clusters in CR acceleration, even in the absence of SNe shocks.

However, shifting the arena of CR acceleration from SNe shocks in the ISM to star clusters has not quite yielded a better estimate of the Neon isotope ratio. For this, one needs to estimate the relative contribution of shocks due to stellar winds and SNe shocks towards CR acceleration. This ratio has so far been treated as a free parameter, empirically chosen to fit the observed Neon

\* E-mail: [biman@rri.res.in](mailto:biman@rri.res.in)

isotopic ratio (e.g. Murphy et al. 2016) in the absence of a rigorous theoretical calculation. In order to understand observed anomalous  $^{22}\text{Ne}/^{20}\text{Ne}$  in CRs, several empirical models have been proposed (e.g. Higdon & Lingenfelter 2003; Binns et al. 2008; Prantzos 2012). However, none of these models have discussed the shock energetics and corresponding source of upstream particles (stellar wind and SNe ejecta), which goes into the acceleration process. It has also been pointed out that the  $^{22}\text{Ne}$  yield used in previous studies to explain the observed ratio from SB scenario is likely an overestimate (Prantzos 2012). As an alternative scenario, some studies proposed CR acceleration by SNe shocks in the wind of massive progenitor star. However, these models need some fine-tuning, such as the requirement that SN shocks should be effective only when the shock speed  $\geq 1600 \text{ km s}^{-1}$  (which excludes the possibilities of CR acceleration by SNe shock beyond free-wind region of the progenitor star, for details see e.g. Prantzos 2012). Recently, Kalyashova et al. (2019) have highlighted the importance of massive star clusters to explain the Neon isotope ratio. However, the contribution of SNe ejecta in their calculations has not been discussed. Therefore, although the basic premise of solving the Neon isotope problem by invoking stellar winds in star clusters seems appealing, detailed estimates have not been available, and, in addition, other avenues also appear bleak.

In this paper, we take a fresh look at the Neon isotope problem, using hydrodynamics of winds in star clusters, the latest stellar evolutionary yields (Limongi & Chieffi 2018), with the standard stellar mass function. Recently, using numerical simulations, we have shown that termination shocks of stellar winds from massive stars can accelerate CRs to produce  $\gamma$ -ray luminosity of a similar magnitude, as well as explain the observed X-ray and synchrotron luminosities (Gupta, Nath & Sharma 2018b). In this paper, we investigate the implications of our model to explain Neon isotope ratio. We show that the observed  $^{22}\text{Ne}/^{20}\text{Ne}$  ratio can be achieved if CRs are produced in massive star clusters by the *combined* effects of wind termination shock (WTS) and SN shocks. With 1D numerical simulation, we estimate the fraction of shock energy processed in wind and SNe ejecta for various acceleration scenarios. We find that for compact clusters, WTS can accelerate particles from the wind material before the onset of SNe. We also show that, in the case of SN shock in wind of progenitor star (Prantzos 2012), the reverse shock is as efficient as the forward shock, thereby accelerating both wind material and SN ejecta. We demonstrate that in this case both the forward and reverse shocks are energetically comparable. Therefore, the acceleration of the ejecta material (rich in  $^{20}\text{Ne}$ ) cannot be neglected as is usually done in the literature, and this poses a problem for the  $^{22}\text{Ne}/^{20}\text{Ne}$  abundance ratio.

The implications of this calculation goes beyond the Neon isotope problem. We show that our results imply more than a quarter of the GCRs being accelerated in WTSs of star clusters. The extent of the shocked wind region also allows us to draw important conclusions about the maximum energy of accelerated CRs. We further argue that supernovae remnants (SNRs) and stellar winds in clusters are both linked to massive stars, and therefore the two sites of CR acceleration, namely, WTS and SNe shocks, may be put together on a common platform of CR acceleration in SBs. Isolated SNe remnants would merely represent the lower end of the star cluster mass function, where OB stars number less than two. These lines of argument paint an integrated scenario of CR acceleration that not only solves Neon isotope and other problems, but also rids the standard paradigm of acceleration in SNRs of its generic problems.

The paper is structured as follows. We first characterize and discuss the WTS in Section 2. The numerical set-up is described in

Section 3. In Section 4, we present our main results on the relative contribution of WTS and SNe shocks and estimate the Neon isotope ratio. In Section 5, we draw attention to a few important implications of our calculations for GCRs. Our findings are summarized in section Section 6.

## 2 WIND TERMINATION SHOCK (WTS)

### 2.1 Formation of the WTSs

Consider a star cluster in which most of the massive stars ( $M_* > 8 M_\odot$ ) are located within a radius  $R_c$ . The total mechanical power launched by massive stars from this spherical region of radius  $R_c$  can be written as  $L_w = \dot{M} v_w^2/2$ , where  $v_w$  is the wind velocity and  $\dot{M}$  is the total outflowing wind mass per unit time. Interaction of the collective wind with the parent cloud forms an interstellar bubble. Near the core of this bubble, the wind expands adiabatically and its mass density is  $\rho_w = \dot{M}/(4\pi r^2 v_w)$ . A WTS forms at the location where the wind ram pressure ( $P_{\text{ram}} = \rho_w v_w^2$ ) balances the hot gas pressure ( $P_{\text{in}}$ ) in the bubble. Thus, the radius of the WTS w.r.t. the centre of the star cluster is

$$R_{\text{ts}} \approx \left( \frac{L_w}{2\pi v_w P_{\text{in}}} \right)^{1/2}. \quad (1)$$

This suggests that if a cluster is compact (i.e.  $R_c \ll R_{\text{ts}}$ ) then a WTS can form. We have confirmed this by performing two 3D simulations of star cluster of 12 massive stars (i.e.  $N_{\text{OB}} = 12$ ) with two different core radius  $R_c = 0.5$  and  $5.0$  pc, respectively. The results are shown in Fig. 1 and for numerical set-up, see Appendix A.

The left- and right-hand panels of Fig. 1 show density snapshots in the  $z = 0$  plane at  $2.9$  Myr for compact (left) and loosely bound (right) star clusters. The left-hand panel shows that a compact cluster has formed a coherent WTS as shown by the grey points (the shock Mach numbers are shown by the grey/black points displayed in the horizontal colour palette). This can be understood as follows.

For this set-up, the total wind power of both clusters is  $L_w = N_{\text{OB}} \times 10^{36} \text{ erg s}^{-1} \approx 1.2 \times 10^{37} \text{ erg s}^{-1}$  and wind velocity is  $v_w = (2L_w/\dot{M})^{1/2} \approx 2000 \text{ km s}^{-1}$ . Taking the hot gas pressure  $P_{\text{in}} \sim 10^{-10} \text{ dyn cm}^{-2}$  (as observed in SBs, see e.g. table 7 in Lopez et al. 2014), from equation (1) we obtain  $R_{\text{ts}} = 3.2$  pc. In the left-hand panel, since the stars are distributed in a region smaller than  $3.2$  pc (see the zoomed-in sub-plot), a WTS has formed.<sup>1</sup> In contrast, the right-hand panel shows that the stars are distributed much beyond  $3.2$  pc, and there is no coherent WTS. We have also confirmed this for the clusters of mass  $\gtrsim 10^3 M_\odot$ . Therefore, compact star clusters can form WTS.

### 2.2 Mach number of WTSs

In the case of compact clusters, the physical properties of the wind (e.g. density, velocity, and pressure profiles) in the region  $r < R_{\text{ts}}$  are similar to the model of Chevalier & Clegg (1985). For  $r \geq R_{\text{ts}}$ , there is a shocked wind region, which is separated from the ambient medium via a contact discontinuity (for details, see Weaver et al. 1977). In order to determine the Mach number of the WTS, we need to know the shock velocity and the upstream wind (free-wind)

<sup>1</sup>In this calculation, we have assumed that wind mechanical power of each star remains steady. In case of episodic winds, there will be internal shocks in the collective wind region but they will not affect the qualitative picture of the existence of WTS.

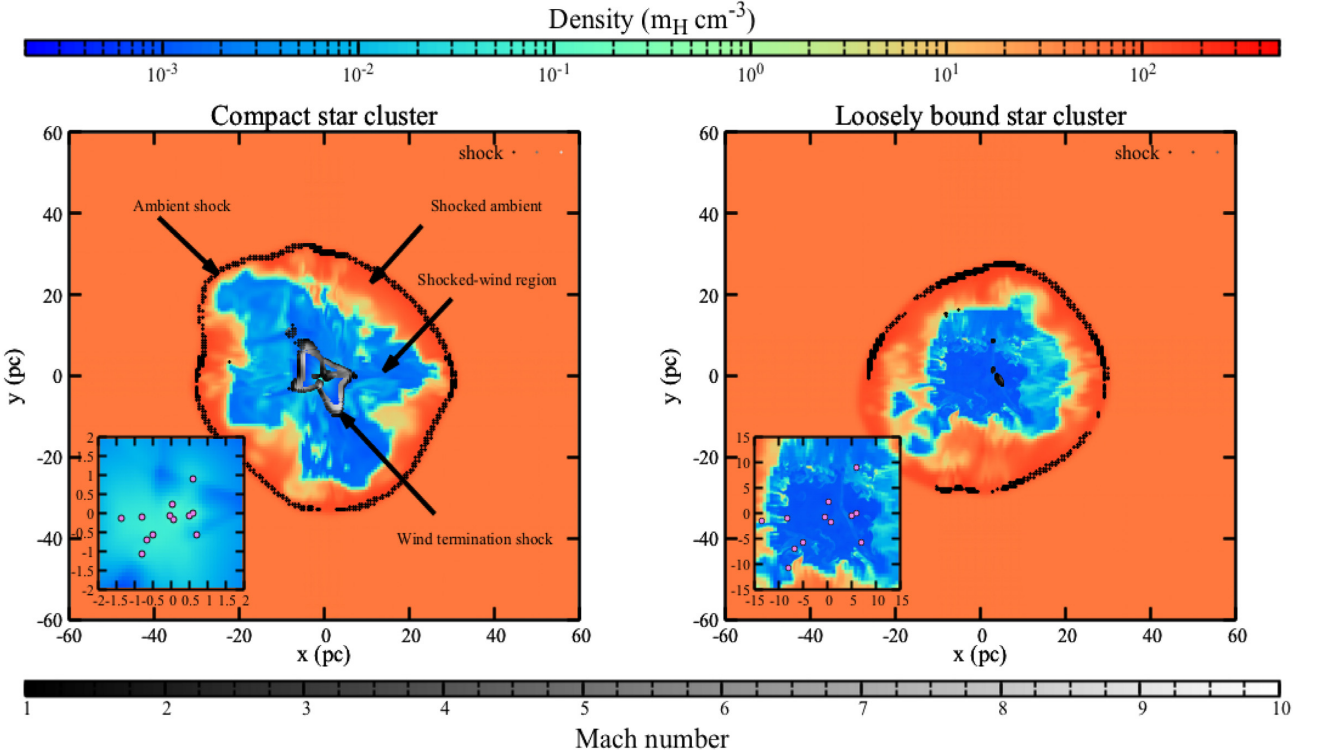


**Figure 1.** Various diagnostics from 3D star cluster simulations for a compact (left) and a loosely bound cluster (right). Snapshots of density (top colour palette) and shock Mach numbers (bottom colour palette) in the  $z = 0$  plane at 2.9 Myr are shown. The sub-plots show the zoomed-in view of the central few pc of the star cluster where the magenta circles denote the locations of the stars after projecting them in the  $z = 0$  plane. The left- and right-hand panels show two different simulations that have identical set-up except for the core radius  $R_c$  of the cluster. For both the left- and right-hand panels, the ambient shocks are weak and appear dark according to the bottom colour palette. The figure shows that a compact star cluster can form a WTS (left-hand panel), and its Mach number is  $\sim 5$ – $10$ , as shown by the bright points.

profile. In the lab frame, the WTS slowly moves outwards (see e.g. equation 9 in Gupta et al. 2018a), the upstream velocity is the same as the wind velocity. The upstream sound speed can be obtained by using table 1 in Chevalier & Clegg (1985). This gives the Mach number of WTS as

$$\mathcal{M} = \frac{v_w}{c_s} = \frac{v_w}{0.56 \dot{M}^{-1/2} L_w^{1/2} (R_{ts}/R_c)^{-2/3}} \simeq 2.5 \left( \frac{R_{ts}}{R_c} \right)^{2/3}. \quad (2)$$

This implies that a large separation between WTS and the cluster core leads to a large Mach number which increases with time as the termination shock moves out.

For a typical cluster of mass  $10^3 M_\odot$  ( $N_{\text{OB}} \approx 12$ ), equation (1) gives  $R_{ts} \approx 3.2 \text{ pc } P_{\text{in},-10}^{-1/2} L_{w,37}^{1/2}$ . The corresponding Mach number of WTS is

$$\mathcal{M} \approx 6 \left( \frac{R_c}{\text{pc}} \right)^{-2/3} \left( \frac{P_{\text{in}}}{10^{-10} \text{ dyn cm}^{-2}} \right)^{-1/3} \left( \frac{L_w}{10^{37} \text{ erg s}^{-1}} \right)^{1/3}. \quad (3)$$

This suggests that compact clusters can have high Mach number WTS. In contrast, the outer shock Mach number is small as seen in Fig. 1.

Although these calculations refer to star clusters, equation (3) is also valid for the wind from a single star. In this case,  $R_c$  can be taken as the radius beyond which the wind becomes supersonic. This scenario is also applicable for bigger star clusters (i.e. core radius  $\gg R_{ts}$ ) in which a global WTS may not form (as shown in the right-hand panel of Fig. 1). In this case, individual stars can

accelerate CRs in their WTS. We discuss these cases separately in Section 4.1.4.

### 3 NUMERICAL SET-UP

The central result of this work is to compare the energy efficiency in accelerating wind material, SNe ejecta, and ambient matter by the WTS and SNe shocks. For this purpose, we need to quantify the fraction of upstream energy that is encountered by wind material, SNe ejecta, and ambient matter. In order to estimate the energy processed at different shocks, we consider four different acceleration scenarios, which can be broadly classified into two categories: (1) isolated SN (Sections 4.1.1 and 4.1.2) and (2) star cluster (Sections 4.1.4 and 4.1.3). In the first case, SN shock expands either in the parent cloud or in the wind of the progenitor star. In the second case, the star cluster may be compact or loosely bound. We have labelled these four acceleration scenarios as Case I to Case IV (for a brief overview see Fig. 2). For each of these cases, we discuss the energetics of various shocks with the help of 1D simulations.

We solve the standard Euler equations in 1D spherical geometry. We use uniformly distributed grids with spatial resolutions  $\Delta r = 0.01 \text{ pc}$  for the Case I, II and  $\Delta r = 0.04 \text{ pc}$  for the Case III, IV, respectively. In order to include the effect of stellar winds/SNe, we consider a spherical region of radius  $r_{\text{inj}}$  within which we inject mass and energy uniformly. Depending on the acceleration scenario that we wish to study,  $r_{\text{inj}}$  ranges from 0.05 to 15 pc. The SN shock is launched by injecting thermal energy  $E_{\text{SN}} = 10^{51} \text{ erg}$  and mass  $M_{\text{ej}} = 10 M_\odot$  in a region of radius 0.05 pc (0.25 pc) for cases I and

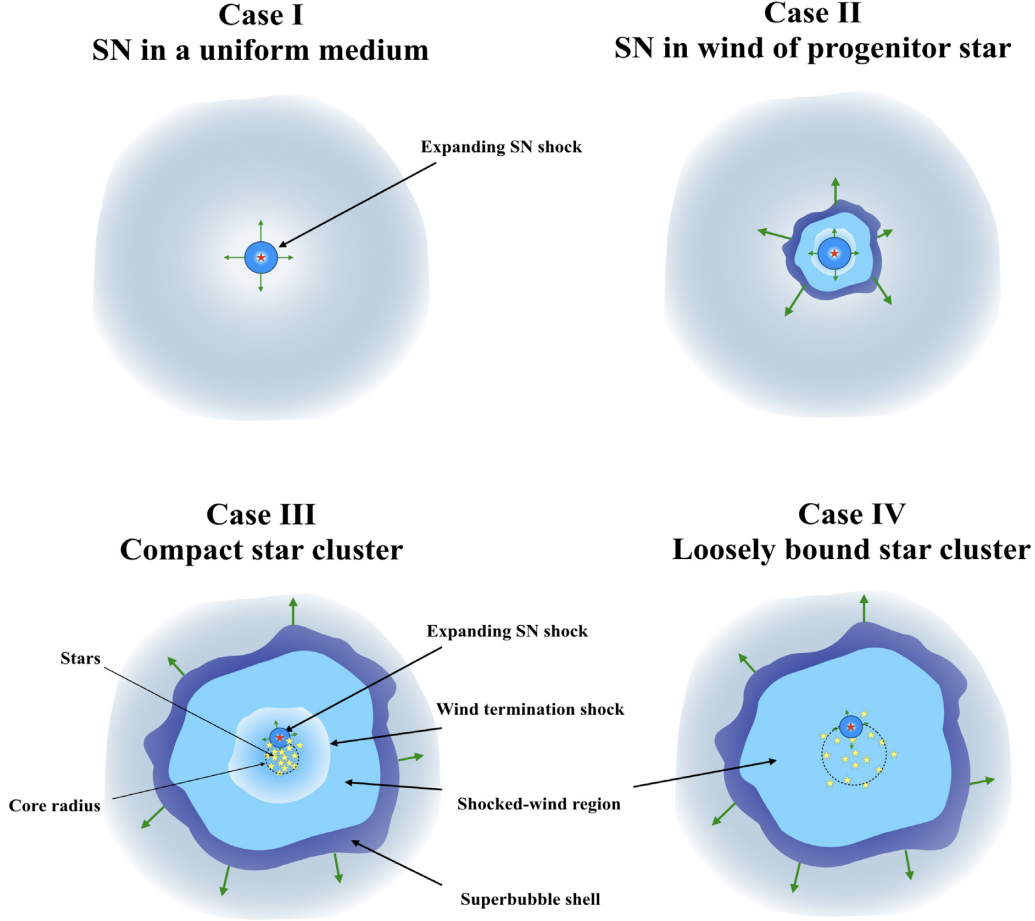


**Figure 2.** Schematic diagram of four different CR acceleration scenarios.

II (cases III and IV). For cases II, III, and IV, the first SN occurs at 3.5 Myr, which corresponds to the main-sequence lifetime of  $\sim 100 M_{\odot}$  star. The cases III and IV represent clusters of mass  $10^4 M_{\odot}$  with two different core radii: 1 and 15 pc, respectively. For these two cases, the time between two consecutive SN explosions is  $\Delta\tau_{\text{SN}} = \tau_{\text{cluster}}/N_{\text{OB}}$ , where  $N_{\text{OB}} \simeq 109$  and  $\tau_{\text{cluster}} \approx 30$  Myr is typical cluster lifetime. For all cases, we assume the initial ambient density  $\rho = 10 m_{\text{H}} \text{ cm}^{-3}$ , and pressure  $10^{-12} \text{ dyne cm}^{-2}$ . Radiative cooling has been included using a tabulated cooling function (Sutherland & Dopita 1993). We have used three passive scalars to distinguish wind, SN ejecta, and ambient matter. These passive scalars help us to identify the material(s) available in the upstream/downstream region of a shock. This is required to find the energy that goes into different types of material: wind, SN ejecta, and ambient matter.

### 3.1 Shock energetics

Various steps in the analysis are described in sections below.

(i) Step 1 – Simulation output: Directly obtained from our hydro runs.

(ii) Step 2 – Shock detection: The following three conditions are used to identify the shocked zones.

$$\nabla \cdot \mathbf{v} < 0, \quad (4)$$

$$\nabla p \cdot \Delta r / p > \delta_{\text{threshold}}, \text{ and} \quad (5)$$

$$\nabla T \cdot \nabla \rho > 0. \quad (6)$$

Here  $\rho$ ,  $p$ , and  $T$  are the density, pressure, and temperature of the fluid. The first condition selects compressed zones. The second condition sets a threshold in pressure jump ( $\delta_{\text{threshold}} = 0.5$ ), and the third conditions helps to avoid contact discontinuity. We have confirmed that these conditions robustly identify shocked zones.

(iii) Step 3 – Identifying upstream/downstream parameters: For each shocked zone, the program compares density, pressure, and sound speed of four to eight neighbouring zones on both sides of the shocked zone. Finally, it gives the density, pressure, and sound speed of the upstream and downstream regions.

(iv) Step 4 – Next we determine the following entities.

(a) Density compression ratio:  $\rho_2/\rho_1$ .

(b) Pressure jump:  $p_2/p_1$ .

(c) Upstream sound speed:  $c_1 = (\gamma p_1/\rho_1)^{1/2}$ , where  $\gamma = 5/3$ .

(d) Upstream Mach number:  $M_1 = \frac{1}{(2\gamma)^{1/2}} \left[ \frac{p_2}{p_1} (\gamma + 1) + (\gamma - 1) \right]^{1/2}$ .

(e) Mass flux:  $\dot{\rho}_m = \rho_1 v_1 = \rho_1 (c_1 M_1) = \rho_2 v_2$ .

(f) Energy flux:  $\dot{\rho}_e = [(5/2)p_1/\rho_1 + v_1^2/2]\rho_1 v_1 = [(5/2)p_2/\rho_2 + v_2^2/2]\rho_2 v_2$ .

Finally, we obtain the total mass/energy flux that crosses the shock surface. This is estimated by multiplying the flux with the shock surface area. In numerical simulations, since the shock surface is

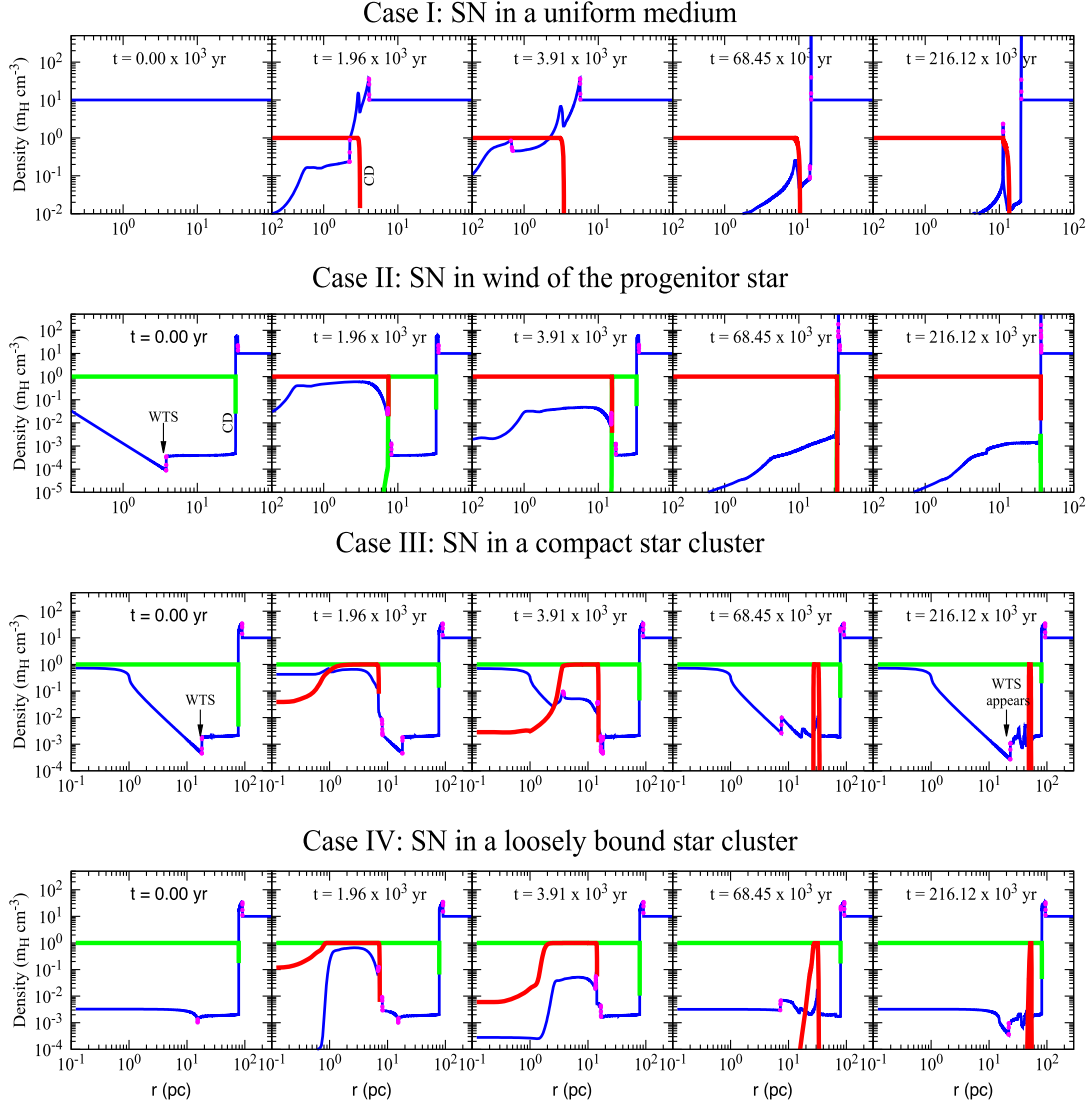


**Figure 3.** Four different CR acceleration scenarios: in all panels, the blue curve represents density profiles, where time  $t = 0$  denotes the epoch of SN explosion. The green and red curves display tracer of wind material and SN ejecta, respectively. Four different acceleration scenarios, which are labelled by Case I to Case IV, are described as follows. Case I: explosion of an isolated star in a uniform medium ( $t = 0 \Rightarrow t_{\text{dyn}} = 0$ ), Case II: explosion of an isolated star in wind of the progenitor star ( $t = 0 \Rightarrow t_{\text{dyn}} = 3.5$  Myr), Case III: SN explosion in a compact star cluster ( $t = 0 \Rightarrow t_{\text{dyn}} = 3.5$  Myr), Case IV: SN explosion in a medium made by a loosely bound star cluster ( $t = 0 \Rightarrow t_{\text{dyn}} = 3.5$  Myr).

made of more than one zone, we have calculated the shocked-zone averaged entities by using the following equations:

$$\dot{m}_T = \frac{\sum_i \dot{\rho}_{m,i} A_i}{\sum_i Z_i}, \quad \text{and} \quad \dot{e}_T = \frac{\sum_i \dot{\rho}_{e,i} A_i}{\sum_i Z_i}, \quad (7)$$

where  $i$  denotes the effective shocked zones where the analysis is performed,  $A_i = 4\pi r_i^2$  is the shock area, and  $\sum_i Z_i$  is the total number of zones in a shock surface (typically  $\sum_i Z_i \approx 4-8$ ). The net flow of mass/energy through the shock surface are calculated using

$$m_T = \int_i dt \dot{m}_T, \quad \text{and} \quad e_T = \int_i dt \dot{e}_T. \quad (8)$$

Note that, the computational domain may contain more than one shock surface encountered by the same material at different

locations. In this case, we have to find zone averaged entities for each shock surface separately (e.g.  $\sum_{\text{shock}} \dot{m}_T$ ). In order to do this, we define a critical distance  $r_{\text{cri}} = 8\Delta r$  (i.e. the length of shock analysis domain), to specify the minimum distance between two shock surfaces. When the separation between two neighbouring shocked zones is smaller than  $r_{\text{cri}}$ , they are considered as the part of the same shock surface.

## 4 RESULTS

The results of our shock analysis program for the cases I, II, III, and IV are discussed below. For a brief overview, see Fig. 2.

Fig. 3 shows the density profiles at five different epoch for four different cases. Panel I shows the classical results of SN in a uniform medium (Case I). The magenta dots show the position of forward and reverse shock of the blast wave. The red curves show that the SN ejecta reaches up to the contact discontinuity (hereafter, CD).

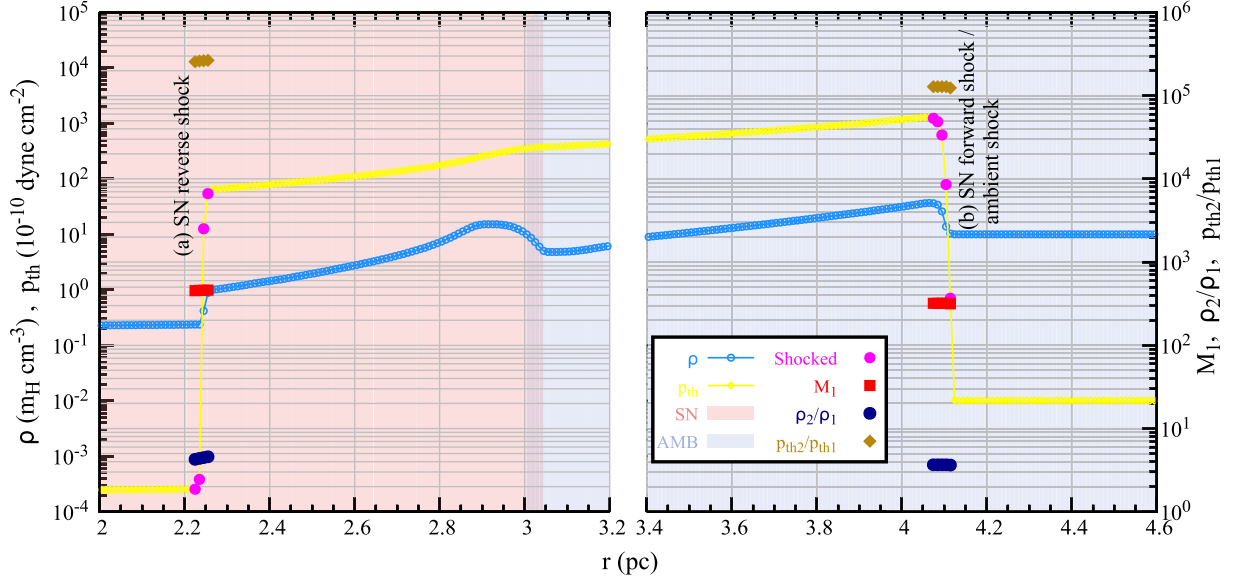


**Figure 4.** Shock diagnostics for an isolated SN in a uniform medium (case I). The left- and right-hand panels display the zoomed-in view of density (blue) and pressure (yellow) profiles of the blast wave near the reverse shock (left) and near the ambient forward shock (right), respectively, at  $t = 1.96 \times 10^3$  yr. The shock profiles shown here represent the second panel of case I in Fig. 3. The background colours of this figure display the tracer of SN ejecta (light red) and ambient matter (light steel blue). The right axis shows the upstream Mach number  $M_1$  (red squares), density jump  $\rho_2/\rho_1$  (dark blue circles), and pressure jump  $p_2/p_1$  (brown diamond symbols). The right-hand panel (for the forward shock) shows that  $M_1 \approx 300$ ,  $p_2/p_1 \approx 1.2 \times 10^5$ , and  $\rho_2/\rho_1 \approx 4$ , which are consistent with our analytical estimates.

For Case II, the first panel shows the density profile just before the SN, where position of the WTS is marked by an arrow. The green curves show that wind material reaches up to the CD. When the SN shock reaches WTS and collides with it, the WTS disappears. In contrast, in Case III, the WTS appears again due to the winds from remaining stars. For Case IV, although we see shocked zones at WTS, it is weak compared to that of case III because the separation between WTS and core radius is small (see e.g. equation (2)). Note that, in the rightmost panel of Case I, II ( $t = 216.12 \times 10^3$  yr), the interior of the bubble contains SN ejecta. In contrast, in the Case III and Case IV, SN ejecta is accumulated near the swept-up ISM (shell) and the interior of the bubble is filled with wind material.

#### 4.1 Shock energetics

We have described each of these cases in detail in the following sections. Note that, each section contains two figures. The first figure shows zoomed-in shock profiles (i.e. Figs 4, 6, 8, and 10), where the blue curves stand for density and yellow curves for pressure. The second figure in each section shows the time evolution of mass/energy of the material that is swept up by the shock (i.e. Figs 5, 7, 9, and 11), where green/cyan stands for wind material, red/light red denotes SN ejecta and dark blue/light steel blue stands for ambient matter.

##### 4.1.1 Case I: SN in a uniform medium

For an SN in a uniform medium, we have used the blast wave solution (e.g. Truelove & McKee 1999) to check our analysis program. For our set-up (i.e.  $E_{\text{SN}} = 10^{51}$  erg,  $M_{\text{ej}} = 10 M_{\odot}$ , and  $\rho = 10 m_{\text{H}} \text{ cm}^{-3}$ ), at  $t = 1.96 \times 10^3$  yr,  $R \approx 4.2$  pc, and  $\dot{R} \approx 840 \text{ km s}^{-1}$ . Therefore, we expect the shock Mach number  $M_1 \approx 840/3 = 280$ , pressure jump  $p_2/p_1 = (5/4)M_1^2 \approx 10^5$ , and

compression ratio  $\rho_2/\rho_1 \approx 4$ . Our shock analysis program confirms this, as shown in Fig. 4.

Fig. 4 shows the zoomed-in density (sky blue) and pressure (yellow) profiles of a blast wave near the reverse shock (left) and the forward shock (right). The magenta points show the shocked zones. Two background colours, i.e. light red and light steel blue, represent the tracers of SN ejecta and ambient matter, respectively. In the left-hand panel, the transition between these two colours represent the location of the CD.

The top/bottom panels of Fig. 5 show various diagnostics of mass/energy that passes through the shock surfaces calculated using equations (7) and (8). The blue and red curves stand for ambient matter and SN ejecta, respectively. The sky blue solid curves represent the analytical predictions. The bottom right panel shows that the reverse shock energy is smaller than the forward shock by a factor of 10. Therefore, the acceleration of SN ejecta is energetically not preferred in this scenario. In this case, the shock energy is mainly encountered by the ambient matter.

##### 4.1.2 Case II: SN in wind of the progenitor star

In this case, the stellar wind of the progenitor star has been included. Before the SN explosion, interaction of the wind with the ambient medium forms a wind bubble. This wind bubble has four distinct regions: (i) free wind, (ii) WTS, (iii) shocked wind region, and (iv) swept-up ambient shell (Weaver et al. 1977). In this case, the WTS can accelerate the wind material even before the SN. When SN occurs, the blast wave moves through these four regions mentioned above. We show the shock profiles in Fig. 6.

In the WTS rest frame, the upstream fluid moves with velocity  $v_w$ , and therefore the mass and energy flux that pass through the WTS are roughly equal to the stellar wind mass-loss rate (i.e.  $\dot{m}_{\text{T}} = \dot{M} = 8 \times 10^{-7} M_{\odot} \text{ yr}^{-1}$ ) and wind power ( $\dot{e}_{\text{T}} = L_{\text{w}} = 10^{36} \text{ erg s}^{-1}$ ), as shown

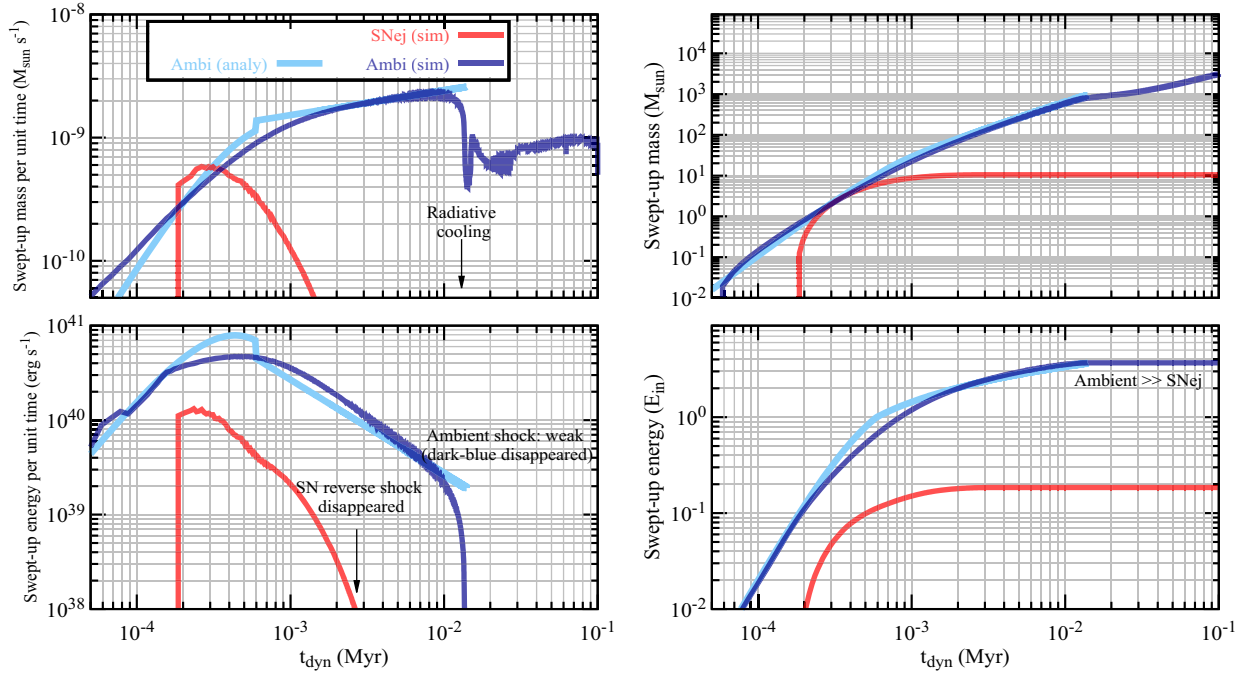


**Figure 5.** Various diagnostics from an isolated SN simulation (Case I). The left-hand panels display the net mass/energy that passes through the shock surface per unit time. The right-hand panels display the time-integrated entities corresponding to the left-hand panels. In the bottom right panel, the vertical axis is normalized w.r.t. the input energy (i.e.  $E_{\text{in}} = 10^{51}$  erg). The sky blue solid curves display analytic predictions (representing forward shock), and blue (ambient)/red (SN ejecta) curves show the results from our analysis. The top right panel shows that the mass swept up by the reverse shock is equal to ejecta mass  $M_{\text{ej}} \approx 10 M_{\odot}$  as expected. The bottom right panel shows that the reverse shock is energetically sub-dominant compared to the forward (ambient) shock of the blast wave. In this case, acceleration of the ambient matter is energetically dominant, with only 5 per cent of the total shock energy processed by the SN ejecta. Note that, the energy swept up in the ambient medium is larger than unity because our calculation does not include the loss of upstream energy due to deceleration of the shell (see e.g. equation 5 in Dermer & Powale 2013).

in the left-hand panel of Fig 7. The shock evolution at different epochs are described below.

(i) The WTS sweeps up stellar wind material until 3.5 Myr (green curves in the left-hand panel). It also confirms the analytic prediction (yellow curve).

(ii) After SN explosion, the forward shock of the blast wave moves in the free wind region. In this phase, the wind material (green) is swept up by both WTS and SN forward shock. This can be seen from the sudden rise in the green curve at 3.5 Myr. However, this phase lasts for a short time, typically  $\approx 900$  yr from the epoch of explosion. The Galactic CR acceleration paradigm that considers SN blast wave in the wind of massive stars mostly focuses on this phase (e.g. Biermann & Cassinelli 1993; Prantzos 2012). However, there are phases described below, which are also important and should not be neglected.

(iii) When the SN forward shock reaches the WTS, it collides with WTS and the WTS disappears. At this moment, a reflected shock and a transmitted shock are formed. The (transmitted) SN forward shock moves through the hot shocked-wind region where it sweeps up the wind material. During this time, the shock energy processed by the wind material is larger than that by the SN ejecta (in the bottom left panel, the green curve is above the red curve). This phase continues as long as the SN forward shock does not reach the CD of wind bubble (until  $\approx 7500$  yr from the epoch of the SN explosion).

(iv) When (transmitted) SN forward shock reaches the CD, the wind material accumulates near the CD. Acceleration of wind material stops when the SN shock collides with CD. This occurs

after  $\approx 7500$  yr from the epoch of SN explosion (see green curves in left-hand panels disappear after  $\approx 3.5075$  Myr).

(v) The collision between the SN forward shock with shocked ambient medium again forms a transmitted shock and a reflected shock. The transmitted shock moves through the ambient medium. This can be noticed in the left-hand panels where dark blue curves suddenly appear after 3.5 Myr + 7500 yr.

(vi) The reflected shock and SN reverse shock moves towards the centre of the explosion and continues to sweep up the SN ejecta (see the sudden rise in red curves at  $\approx 3.5075$  Myr). They reach the point of explosion at  $\approx 3.5 \times 10^6 + 2 \times 10^4$  yr and both shocks disappear.

Therefore, in this scenario, the strong shocks remain in bubble for  $\approx 3.5 \times 10^6 + 2 \times 10^4$  yr, much longer than in an isolated SN. The top right panel shows that the swept-up ejecta mass  $\approx 10 M_{\text{ej}}$  (red), as expected. Comparison of the red and green curves in the bottom right panel shows that the shock energy encountered by SN ejecta is *larger* than the wind/ambient material, a point usually missed in discussions of CR acceleration by SN shocks in massive stellar wind.

Note that, in this calculation, we have not considered the time evolution of stellar wind luminosity and mass-loss rate. Depending on the mass of a star, the stellar wind of the progenitor star can evolve with time, which can modify the internal structure of the bubble, even before the onset of an SN explosion (see e.g. Dwarkadas 2007a, b; Telezhinsky, Dwarkadas & Pohl 2013). To investigate this, one needs to perform a similar calculation for each stellar mass, as presented in this section. In Appendix B1, we have studied one

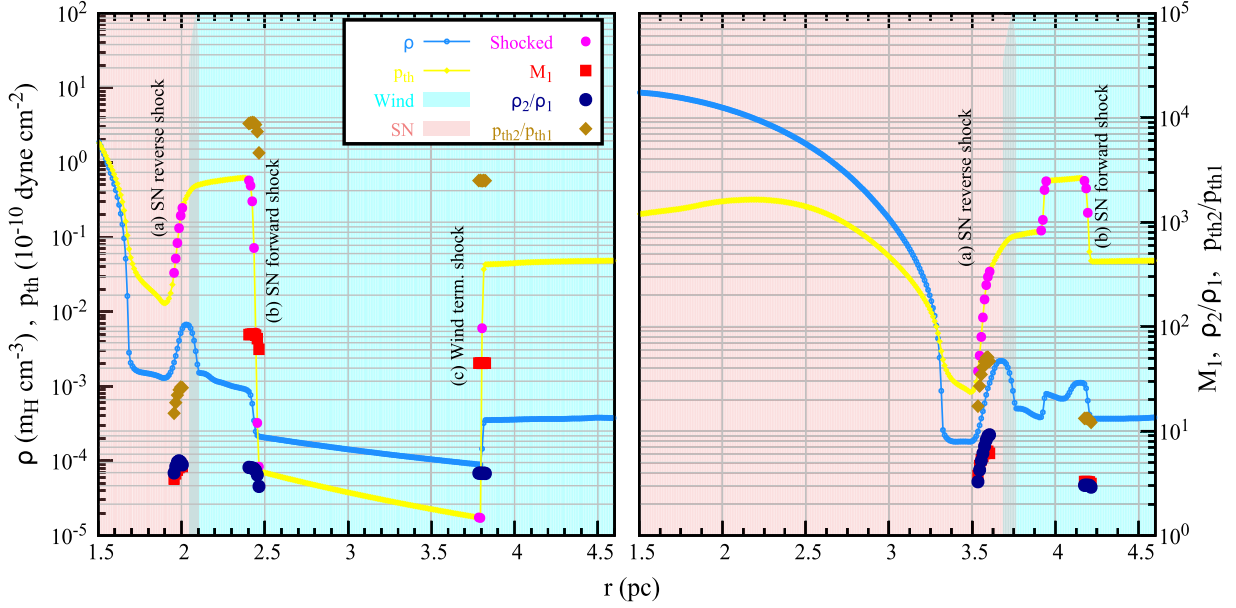


**Figure 6.** The left- and right-hand panels display the zoomed-in view of density (blue) and pressure (yellow) profiles near the WTS at two different times separated by a time interval of  $\approx 300$  yr. The left-hand panel shows a phase when SN shock is propagating in free wind region and the right-hand panel shows just after SN shock hits the WTS. The right axes represent upstream Mach number  $M_1$  (red squares), density jump  $\rho_2/\rho_1$  (dark-blue circles), and pressure jump  $p_2/p_1$  (brown diamond symbols) obtained from the analysis program. The tracer of wind material and SN ejecta are shown by the background colours (light cyan for wind and light red for SN ejecta as in Fig. 4). The left-hand panel contains three distinct shock surfaces: (starting from left) (a) SN reverse shock (sweeping up SN ejecta), (b) SN forward shock (wind material), (c) WTS (wind material). In this case, the wind material encounters *two different shock surfaces* (i.e. shock b, c) whereas the SN ejecta encounters a single shock surface (shock a). As soon as the blast wave forward shock collides with the WTS (i.e. collision between shock b with shock c), the WTS disappears (see the right-hand panel, shock c is absent). Comparison of Mach numbers (red squares) between left- and right-hand panels near the shock (a) shows that the SN reverse shock becomes stronger after the SN forward shock and WTS collide.

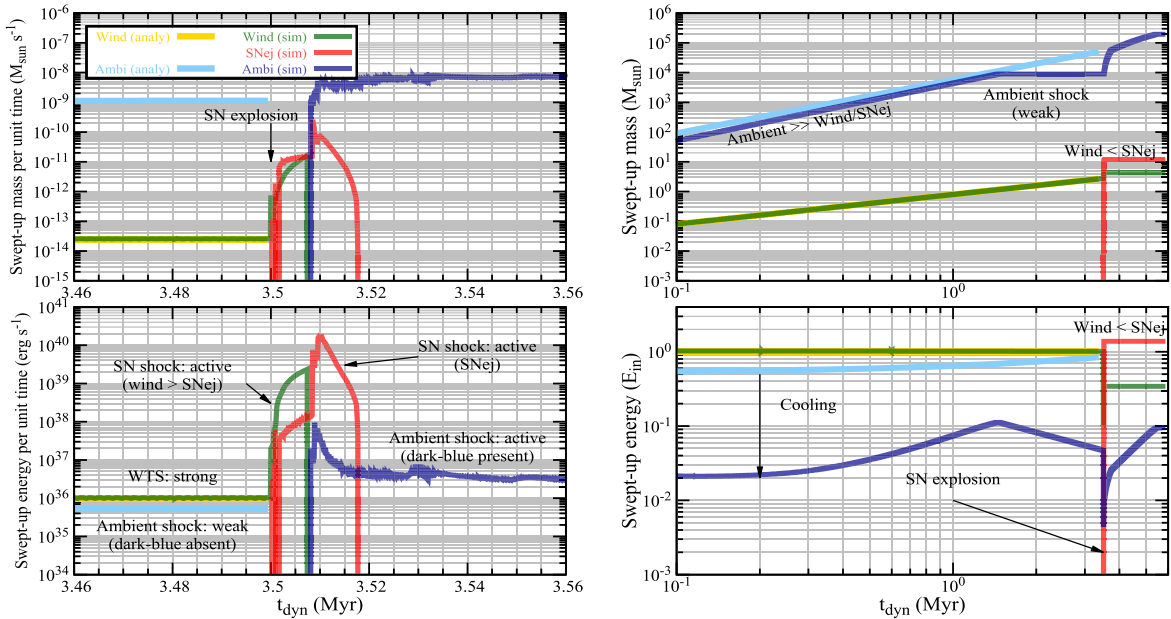


**Figure 7.** Shock diagnostics from an isolated SN in wind of progenitor star (top/bottom panel: mass/energy). Unlike Case I, in this model, we have included stellar wind until 3.5 Myr when the star has exploded. The left-hand panels shows the zoomed-in view of 3.46–3.56 Myr, during the epoch of SN explosion. They display the net mass/energy that passes through the shocked surface per unit time (i.e.  $\dot{m}_T \dot{e}_T$  using equation 7). The right-hand panels display the time-integrated mass (top) and energy (bottom) i.e.  $m_T$  and  $e_T$  (using equation 8). In the bottom right panel, the vertical axis is normalized w.r.t. the total input energy until that epoch. In all panels, the green, red, and blue curves denote wind, SN ejecta, and ambient matter, respectively. The yellow/sky blue solid curves display the expected results from analytic calculation (shown only for WTS and ambient shock).

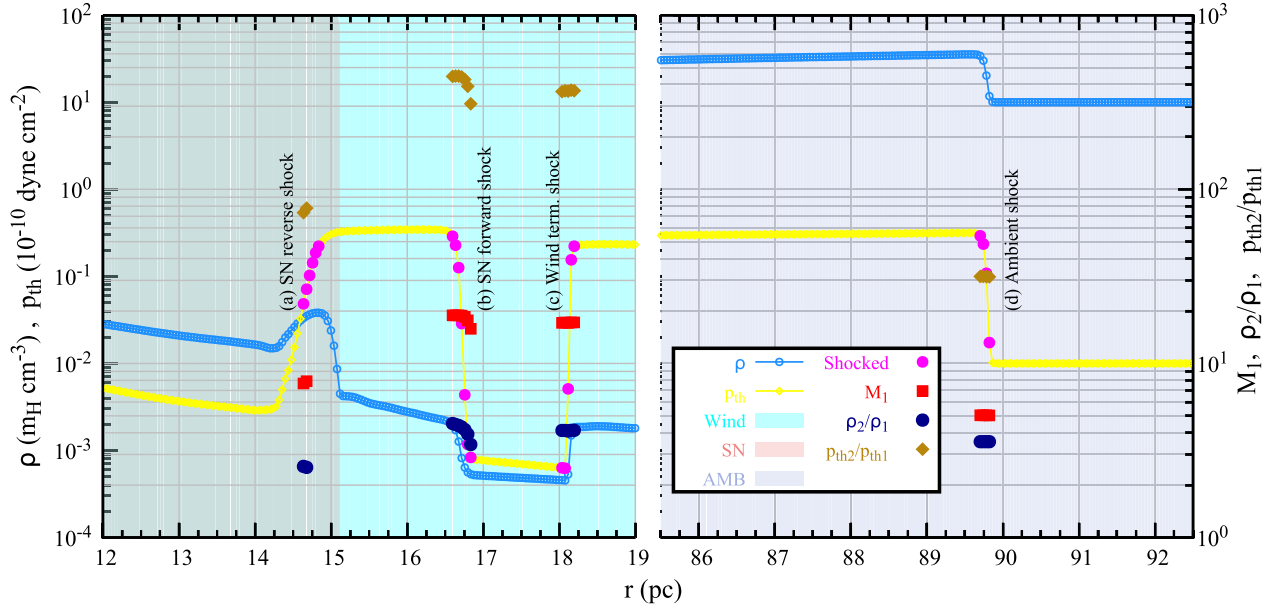


**Figure 8.** The zoomed-in view of density (sky blue) and pressure (light yellow) profiles of an SB near the WTS (left) and ambient shock (right), respectively, at  $t \approx 3.504$  Myr (i.e. immediately after the first SN). The used colour codes are identical with Figs 4 and 6. The figure contains four shocked regions: (starting from left) (a) SN reverse shock ( $M_1 \approx 7$ ; sweeps up wind + SN), (b) SN forward shock ( $M_1 \approx 20$ ; sweeps up wind), (c) WTS ( $M_1 \approx 18$ ; sweeps up wind), and (d) ambient shock ( $M_1 \approx 5$ ; sweeps up ambient material). The figure shows that wind material is swept up at three locations: (a), (b), and (c), whereas the SN ejecta is swept up only at (a). Therefore, in the global energy budget, one can expect the acceleration of SN ejecta to be energetically sub-dominant compared to the wind material.

such case for  $35 M_{\odot}$  star and find that our conclusion qualitatively remains the same.

#### 4.1.3 Case III: compact star clusters

In this case, the stars are close to each other and the wind bubbles of individual stars overlap and generate a collective wind which forms a WTS. This WTS can accelerate the wind material, similar to Case II. When the first SN occurs in the cluster, the forward shock of the blast wave moves outward by sweeping up the wind material. In this case, the free wind is denser than that of a single star (i.e. Case II), and therefore the forward shock of the blast wave spends a longer time in the free wind region.

The shock profiles at  $3.5 \text{ Myr} + 4 \times 10^3 \text{ yr}$  are shown in Fig. 8. The left- and right-hand panels represent the zoomed-in shock profiles near the WTS and ambient shock, respectively. The profiles look similar to Fig 6; however, in this case, the SN reverse shock (labelled shock a) also sweeps up the wind of remaining stars. This can be noticed from the background colour in the left-hand panel of Fig. 8 where the mixing between light red (SN ejecta) and cyan (wind material) has produced a mixed colour (light grey).

Fig. 9 shows the shock energetics of wind material, SN ejecta, and ambient matter as described below.

(i) When the SN forward shock moves through the free wind region, it sweeps up wind material. See the left-hand panels of Fig. 9 where the green curves suddenly rise at 3.5 Myr. In this phase, the SN reverse shock is not strong (in the bottom left panel, the red curve at  $\approx 3.5$  Myr is below the green curve).

(ii) The peak in the green curves at 3.505 Myr represents the epoch of collision between the SN forward shock and WTS. This collision produces a transmitted shock and a reflected shock, similar

to Case II. However, unlike Case II, the transmitted shock that moves in the shocked-wind region may not reach the CD of the SB. This is because of the fact that the size of the bubble is bigger than Case II, the SN forward shock becomes subsonic. Therefore, the shocked ISM shell can remain unaffected. This is shown by dark blue curves in the left-hand panels of Fig. 9.

(iii) The SN reverse shock keeps moving towards the centre of the bubble. However, due to the winds of remaining stars, it cannot reach the central region. Instead, the winds of other stars push the SN reverse shock outwards. In this phase, the shock energy is equally shared by the wind material and SN ejecta (red curves fall on the top of green curves). This phase ends when the SN ejecta accumulate near the CD of the SB (red curves disappear at  $\approx 3.5 \text{ Myr} + 2.5 \times 10^4 \text{ yr}$ ). By this time, the WTS forms again and the acceleration of wind material continues.

(iv) This chain of events repeats as long as the energy deposited by the wind is larger than that of SNe. When the number of SN events in the cluster becomes large, the WTS becomes weak. After that, SNe shocks accelerate both wind material and SNe ejecta.

The bottom right panel of Fig. 9 shows that the fraction of the input energy encountered by the wind material is larger than the SN ejecta by a factor of  $\gtrsim 6$ . Therefore, in this scenario, the acceleration of wind material is energetically dominant.

#### 4.1.4 Case IV: loosely bound star clusters

For loosely bound star clusters, a global WTS may not form. However, the individual stars can have their own WTSs. For a detailed investigation, we need to focus on two different length-scales: (i) a global length-scale (SB;  $\gtrsim 10$  pc), and (ii) a local length-scale that focuses on the individual stars ( $\lesssim 1$  pc).

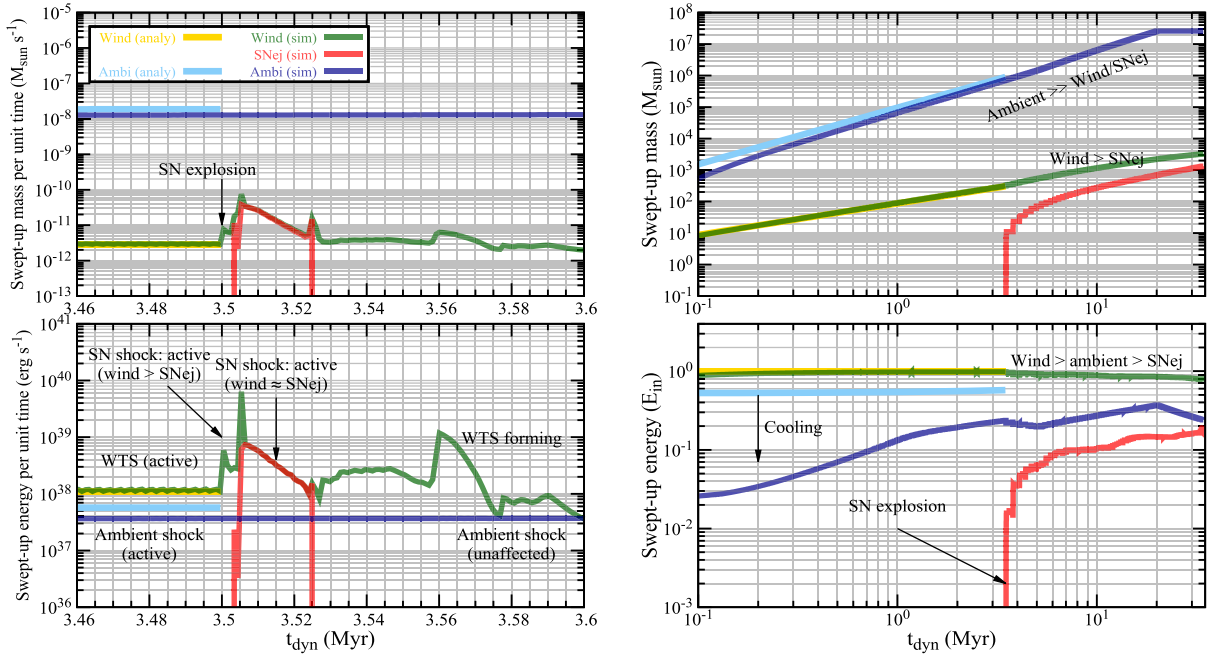


**Figure 9.** Shock diagnostics of a compact star cluster (top panel: mass and bottom panel: energy), similar to Figs 5 and 7. In the bottom right panel, comparison of red and green curves (dashed/solid) shows that the net shock energy going into SN ejecta is *smaller* than that of the wind material by a factor of  $\sim 10$  at  $\gtrsim 10$  Myr.

In the global length-scale, strong shocks appear only when SNe occur in the cluster. The zoomed-in density profiles near the SN forward/reverse shock and ambient shock are shown in Fig. 10. From the epoch of a given SN explosion, since the blast wave moves in a hot bubble, the shock Mach number is small compared to the case of compact star cluster (Case III). This can be seen by comparing the red squares of Figs 8 and 10.

The shock energetics are shown in Fig. 11 and described below:

(i) In the left-hand panels of Fig. 11, the green curves are absent until 3.5 Myr because WTS is absent. The wind material gets accelerated (green curves appear after 3.5 Myr) after the first SN.

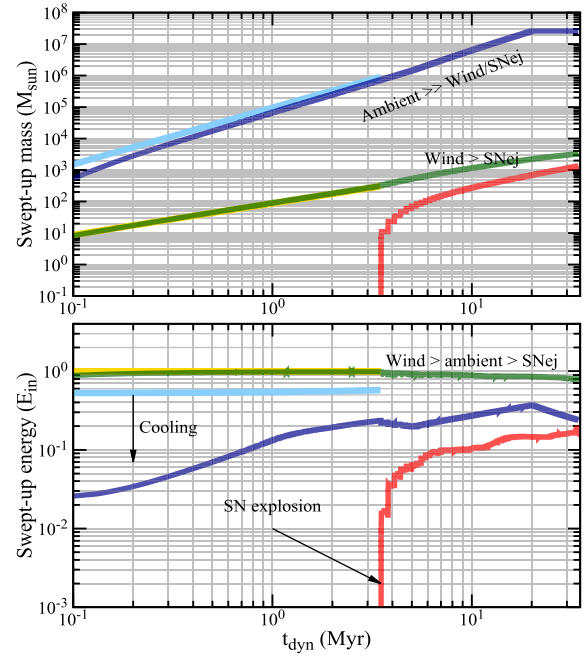
(ii) The wind material is swept up by both the forward and reverse shocks of the SN blast wave, similar to Case III. In this phase, the shock energy mostly goes into wind material (the green curves are above the red curves until 3.5 Myr + 5000 yr).

(iii) Since the bubble is made of hot plasma, the SN forward shock disappears before it can reach the CD of the SB. The SN reverse shock remains active and moves towards the central region of the cluster. The winds of remaining stars push the SN ejecta and accumulate them near the CD of the SB. In this phase, the SN reverse shock energy equally goes to the wind material and SN ejecta (the red curves fall on the top of green curves until 3.5 Myr +  $4 \times 10^4$  yr), similar to Case III.

(iv) When the SN reverse shock completely sweeps up the SN ejecta, the red curves disappear (3.5 Myr +  $4 \times 10^4$  yr). However, the SN reverse shock continues to sweep up the wind material till 3.5 Myr +  $6 \times 10^4$  yr and then it disappears (green curves disappear).

(v) The above scenario repeats itself whenever a star explodes in the cluster.

The bottom right panel of Fig. 11 shows that the shock energy going into SN ejecta is smaller than that into wind material by a factor of  $\sim 2$  (unlike the factor of  $\gtrsim 6$  for compact clusters).



There are some additional physical processes at local length-scale of a loosely bound star cluster. In this case, a star is located in a hot medium made by the winds of other stars. Here, the ambient gas (inside the hot bubble) is mostly dominated by the wind material. This can be seen from Case IV of Fig. 3, which shows that the interior of the bubble is covered by the green curve (a tracer of wind material). In this case, the shock evolution is similar to Case II, although the shock energetics are different. For example, the outer shock of the bubble is weak because the ambient medium is hot. It also makes the bubble size smaller than in Case II. In contrast, the WTS can be as strong as in Case II. We have calculated the shock energetics and found that the shock energy is mostly encountered by the wind material, similar to Case II.

## 4.2 Shock energetics

Let us summarize our findings here regarding the shock energetics, before moving on to the estimate of Neon isotope ratio:

(i) **Isolated SN:** In Case I, i.e. SN explosion in a uniform medium, the SN ejecta is confined inside a blast wave, and therefore can be accelerated by the reverse shock. We have shown that the reverse shock energy is  $\sim 10$  times smaller than that of the forward shock (see bottom right panel of Fig. 5). Therefore, acceleration of SN ejecta is energetically *not* preferred in this case. We expect ISM nuclei to be accelerated more efficiently compared to SN nuclei by a ratio of 10: 1.

In Case II (SN in the wind of a progenitor star), WTS can accelerate the wind material before the SN. When SN occurs, a blast wave moves through the free wind region for a few 100 yr. Eventually, the forward shock of the blast wave collides with the WTS. During this phase, the reverse shock of the blast wave becomes strong (see left-hand panel of Fig. 6) and finally reaches the centre. In contrast, the forward shock of the blast wave moves through the hot bubble

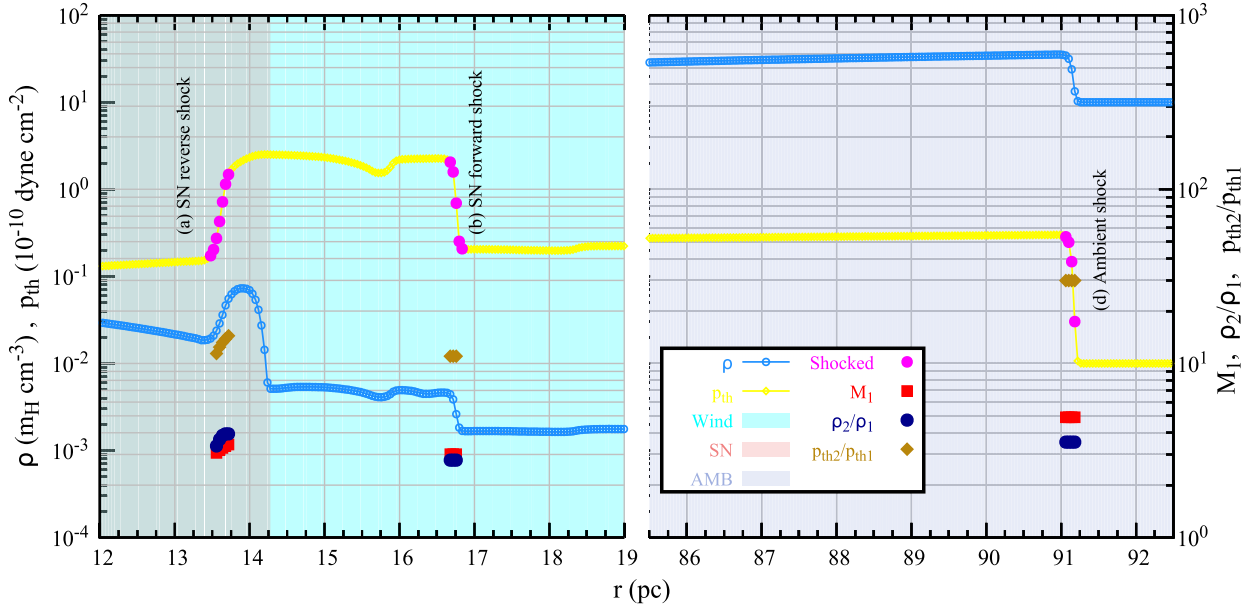


**Figure 10.** The zoomed-in view of density (sky blue) and pressure (light yellow) profiles of an SB near the SN forward/reverse shocks (left) and ambient shock (right), respectively, at  $t \approx 3.504$  Myr (the same epoch as in Fig 8). Unlike Case III (Fig. 8), this figure contains only three shock surfaces: (starting from left) (a) SN reverse shock ( $M_1 \approx 4$ ; sweeping up wind + SN), (b) SN forward shock ( $M_1 \approx 3$ ; sweeping up the wind material), and (d) ambient shock ( $M_1 \approx 5$ ; sweeping up ambient matter), i.e. a global WTS (shock c) is missing. The figure shows that wind material is swept up at the shocks (a) and (b), whereas the SN ejecta is swept up only at (a). Therefore, the shock energy encountered by wind material can be larger than the SN ejecta.

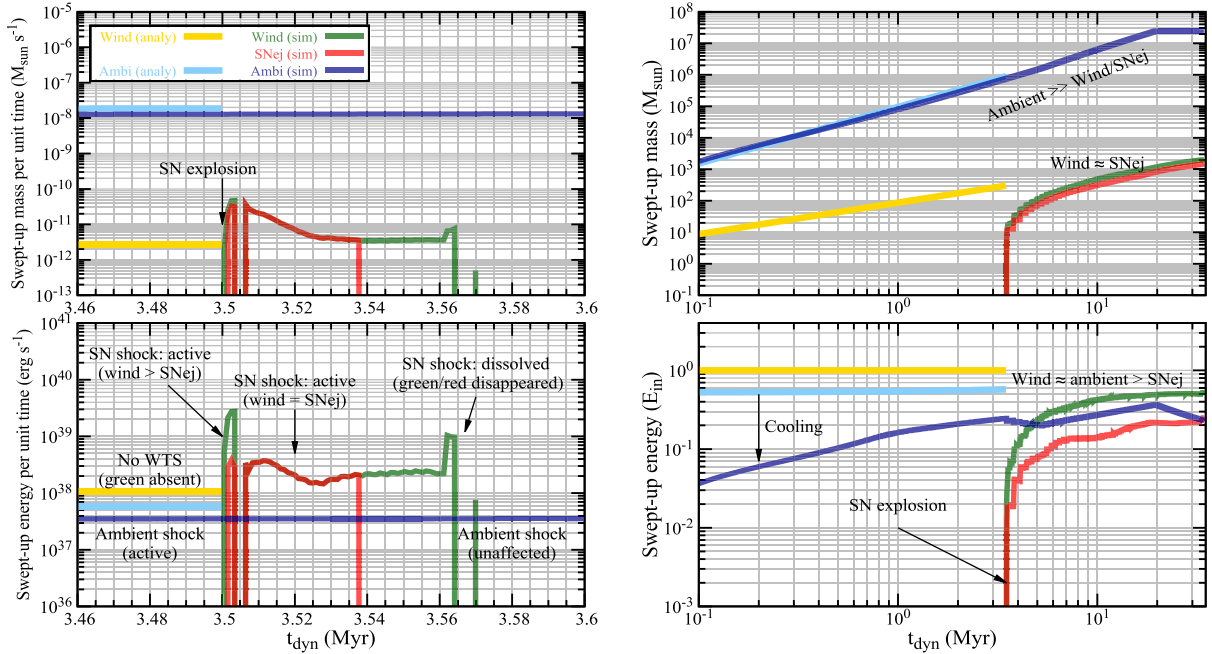


**Figure 11.** Shock diagnostics of a loosely bound star cluster. In this case, the strong shocks appear after the first SN. The description of this figure is similar to Fig. 11. Comparison of the red and green curves in the bottom right panel shows that the shock energy going into SN ejecta is smaller than that into wind material by a factor of  $\sim 2$ .

and hits the wind-driven shocked ISM shell. As the temperature of the bubble is  $\sim 10^7$  K, the SN forward shock is weak compared to the reverse shock (see right-hand panel of Fig. 6). We have estimated the shock energy encountered by the wind material and SN ejecta, and found that both are comparable. Therefore, in realistic calculations, acceleration of SN ejecta should also be considered in addition to the acceleration of the wind material.

(ii) **Star cluster:** In this case, depending on the compactness of the star cluster, stellar winds from the stars can form a coherent WTS. This WTS can accelerate wind material for  $\sim 3$  Myr before any SN. When the first SN occurs in the cluster, the forward shock of the blast wave moves outwards by sweeping up the wind material. A reverse shock develops and sweeps up SN ejecta as well as the winds of remaining stars. When the SN forward shock collides with

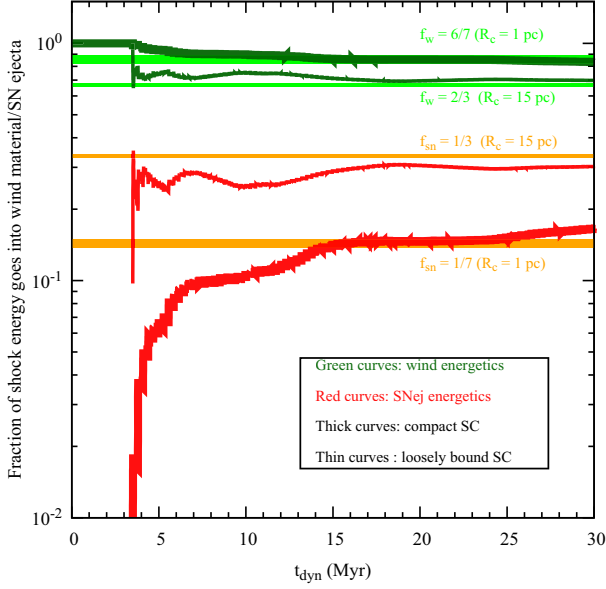


**Figure 12.** Shock energetics of wind material and SN ejecta. The vertical axis shows the fraction of shock energy going into wind material (green) and SN ejecta (red) (equation 9). The thick curves represent the case of compact star clusters ( $R_c = 1$  pc, i.e. Case III) and the thin curves represent loosely bound star clusters ( $R_c = 15$  pc, i.e. Case IV). These curves show that the shock energy encountered by wind material is larger than that by SN ejecta.

the WTS, it becomes weak. After that, it travels through the hot interior and the shock may disappear depending on the size of the bubble. Unlike Case II, the SN reverse shock cannot reach the centre because the remaining stars continuously push it outwards. This process brings the SN ejecta near the CD of the SB. After  $\sim 10^3$ – $10^4$  yr (depending on the compactness, see Figs 11 and 9), the SN reverse shock becomes weak and the winds of remaining stars again form a WTS. This process continues as long as the wind injection dominates over the SN event (until  $\sim 10$  Myr). After that, the wind becomes weak and the SNe start controlling the evolution of the SB. SNe shocks continue to accelerate both wind material and SN ejecta. In the global energy budget, we have found that the shock energy deposited into wind material is larger than that into SN ejecta by a factor of  $\sim 2$ – $6$ , depending on the compactness of the cluster.

Next, we define two parameters to represent the fraction of shock energy processed in the wind material and SN ejecta in clusters,

$$f_w = \frac{E_w}{E_w + E_{sn}} \text{ and } f_{sn} = \frac{E_{sn}}{E_w + E_{sn}}, \quad (9)$$

where  $E_w$  and  $E_{sn}$  denote the total shock energy processed by wind material and SN ejecta, respectively. These factors are shown in Fig. 12 as a function of dynamical time.<sup>2</sup>

This figure shows that  $f_w \approx 2/3$ – $6/7$  and  $f_{sn} \approx 1/3$ – $1/7$ . At early times ( $\lesssim 10$  Myr), the difference is larger than a factor of 10 in case of a compact star cluster. *Therefore, in star clusters, the accel-*

<sup>2</sup>In case of isolated SN (Case I), the fraction of shock energy going into SN ejecta is 5 per cent and to ISM material is 95 per cent (see the bottom right panel of Fig. 5). For Case II of SN in massive stellar wind, these fractions become  $\sim 70$  per cent and  $\sim 5$  per cent, respectively, and the rest  $\sim 25$  per cent goes into wind material (see the bottom right panel of Fig. 7).

*ation of the wind material is energetically preferred than the SN ejecta.*<sup>3</sup>

### 4.3 $^{22}\text{Ne}/^{20}\text{Ne}$ in CRs

Next, we use our results of shock energetics to determine the isotope ratios in CRs, using the stellar evolutionary model of Limongi & Chieffi (2018). The yields of various elements in these models depend on initial metallicities, rotational velocities, and black hole cut-off masses. Our estimates are robust to the variations within the uncertainties of these models. The abundances of  $^{20}\text{Ne}$  and  $^{22}\text{Ne}$  in wind and SN ejecta are shown in Fig. 13. In the rightmost panel, the curves indicate that  $^{22}\text{Ne}/^{20}\text{Ne}$  ratio is large in the winds of massive stars (and to some extent, the SN ejecta of  $\lesssim 20 M_\odot$  progenitors). The green line shows the corresponding ratio in GCRs. Note that there are some difference in the ratios of  $^{22}\text{Ne}/^{20}\text{Ne}$  between rotating and non-rotating models.

Denoting the masses of elements  $^{22}\text{Ne}$  and  $^{20}\text{Ne}$  by  $m^{22}\text{Ne}$  and  $m^{20}\text{Ne}$ , respectively, we estimate the isotopic ratio of  $^{22}\text{Ne}/^{20}\text{Ne}$  as follows. Various steps of the calculation are summarized in Fig. 14. Since the number of CRs accelerated is expected to be proportional to the energy crossing the shock, we calculate energy weighted wind and SN yields making use of shock energy deposited in wind material and SN ejecta, as calculated in Section 4.2. The instantaneous isotopic ratio of  $^{22}\text{Ne}/^{20}\text{Ne}$  in SB is

$$\left( \frac{m^{22}\text{Ne}}{m^{20}\text{Ne}} \right) = \frac{f_w \left\{ \int_{t'=0}^t dt' \left( \sum_{i=1}^{(N_w-SN)} \dot{m}_w^{22}\text{Ne}(t') \right) \right\} + f_{sn} \left\{ \sum_{i=1}^{SN} m_{sn}^{22}\text{Ne} \right\}}{f_w \left\{ \int_{t'=0}^t dt' \left( \sum_{i=1}^{(N_w-SN)} \dot{m}_w^{20}\text{Ne}(t') \right) \right\} + f_{sn} \left\{ \sum_{i=1}^{SN} m_{sn}^{20}\text{Ne} \right\}} \quad (10)$$

The time average ratio of  $^{22}\text{Ne}/^{20}\text{Ne}$  that is accelerated up to time  $t$  in SB (Prantzos 2012) is obtained using

$$\left( \frac{^{22}\text{Ne}}{^{20}\text{Ne}} \right)_{\text{CR}} = \frac{1}{t} \int_{t'=0}^t dt' \left( \frac{m^{22}\text{Ne}}{m^{20}\text{Ne}} \right). \quad (11)$$

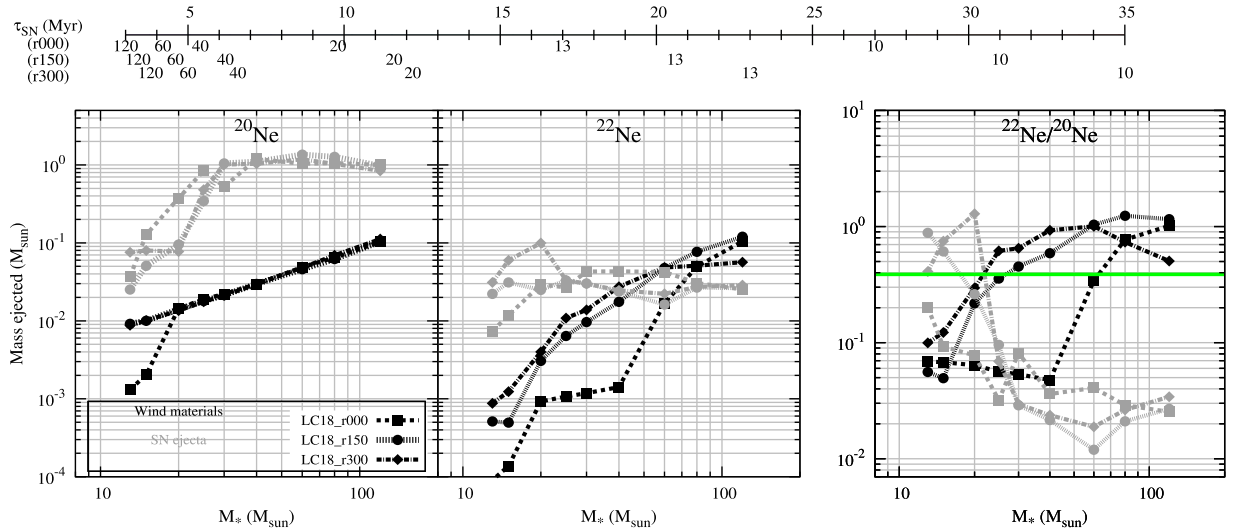
These ratios for different stellar parameters are shown in Fig. 15.

Fig. 15 shows that the ratio of  $^{22}\text{Ne}/^{20}\text{Ne}$  is dominated by the abundance ratio in the stellar wind material. Initially, the ratio is small because the wind of massive stars is dominated by  $^{20}\text{Ne}$  except in the pre-SN wind of stars with mass  $\geq 20$ – $60 M_\odot$ , which begin to appear only after  $\sim 3$  Myr. Therefore,  $^{20}\text{Ne}$  produced in SN ejecta and winds of lower mass stars remain sub-dominant in CRs. After  $\sim 10$  Myr, the cluster is left with stars ( $\leq 20 M_\odot$ ) that contribute little to  $^{22}\text{Ne}$  and  $^{20}\text{Ne}$ , and the isotope ratio remains practically frozen at the value attained by this time. Although a clear enhancement of  $^{22}\text{Ne}/^{20}\text{Ne}$  has been observed in our analysis, it is worth mentioning that the stellar yields depend on the assumption of rotational speed of massive stars. We also note that since the acceleration of ejecta material is energetically less efficient, other isotope ratios such as  $^{59}\text{Ni}/^{59}\text{Co}$  are likely to be small in GCR, as observed (Wiedenbeck et al. 1999).

## 5 DISCUSSIONS

We have therefore been able to calculate the relative contribution of WTS and SNe shocks in star clusters, and their role in enhancing

<sup>3</sup>Also see Appendix B, which shows that the shock energy deposited into wind material is larger than that into SN ejecta by a factor of  $\sim 2$ – $6$  even when one considers a time-dependent wind model.



**Figure 13.** Stellar wind (black) and SN (grey) yields for different stellar masses. The three line styles – dashed, dotted, and dash–dotted – represent three stellar models where initial rotational speed are 0, 150, and 300  $\text{km s}^{-1}$ , respectively. The top horizontal bar shows the epoch of SN explosion for some selective stellar masses ( $M_*$  in the unit of  $M_\odot$ ) for three different initial rotational speeds (e.g. the label *r300* represents the rotational speed 300  $\text{km s}^{-1}$ ). In rightmost panel, the green line shows the observed  $^{22}\text{Ne}/^{20}\text{Ne}$  in GCRs.

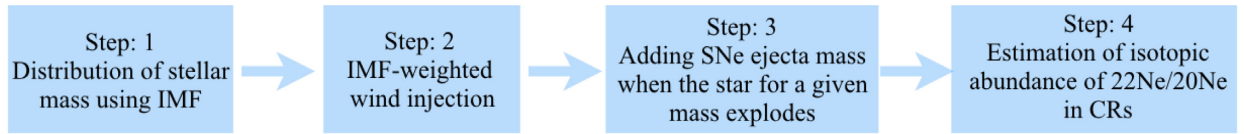


**Figure 14.** Various steps to estimate  $^{22}\text{Ne}/^{20}\text{Ne}$  ratio in CRs accelerated in star clusters.

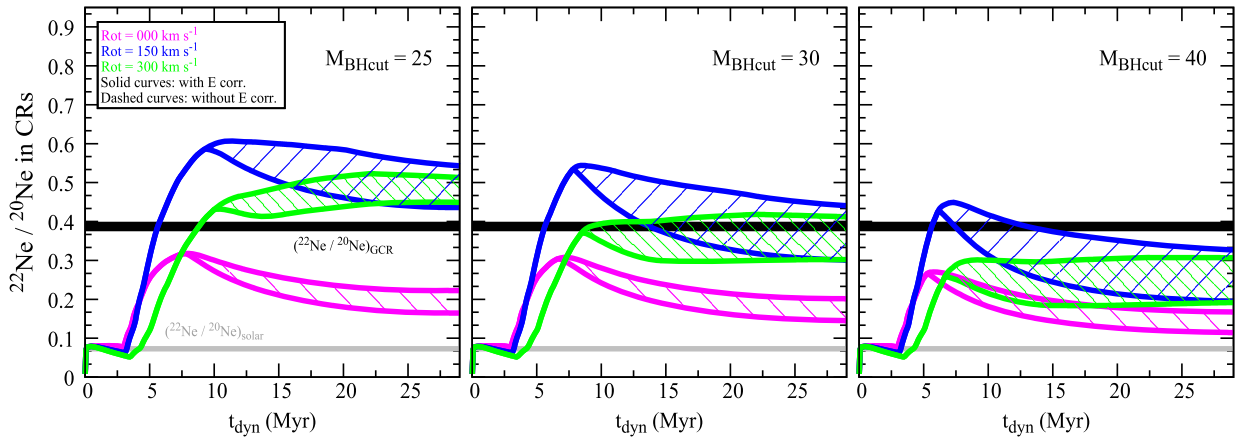


**Figure 15.** Time evolution of  $^{22}\text{Ne}/^{20}\text{Ne}$  in CRs from star clusters. The three panels show the result for models with different black hole cut-off mass ( $M_{\text{BHcut}} = 25, 30, \text{ and } 40 M_\odot$ ). The three colours – magenta, blue, and green – represent different stellar models with initial rotation speed 0, 150, and 300  $\text{km s}^{-1}$ , respectively. The black and grey solid lines display the  $^{22}\text{Ne}/^{20}\text{Ne}$  ratio observed (Binns et al. 2008) in GCR and in the solar wind, respectively. The dashed curves show the  $^{22}\text{Ne}/^{20}\text{Ne}$  ratio without energy correction, i.e. acceleration of both wind material and SN ejecta are considered to be equally probable. The solid curves show the same ratio, after taking the energy weightage 6/7 and 1/7 for wind material and SN ejecta, respectively (see Fig. 12). The solid curves show that after energy correction, the time dependence of  $^{22}\text{Ne}/^{20}\text{Ne}$  becomes weak and the values can be reconciled with observations.

the Neon isotope ratio to the observed label. This match with the observed ratio encourages us to speculate on the implications of our calculation.

### 5.1 Common platform for WTS and SNe shocks

To begin with, our calculations make use of both SNe shocks and WTSs in star clusters. It may appear that isolated SNRs, which are

considered as the standard sites of CR acceleration, have no relation with star clusters. However, star clusters provide the necessary ingredients for an integrated picture of both sources (SN shocks and WTSs), considering the fact that massive OB stars form in dense, compact (of pc scale) clusters (Pfalzner 2009; Portegies Zwart, McMillan & Gieles 2010). Although massive stars are sometimes found outside clusters, as in LMC (Sana 2013), they can be considered to be ‘slow runaways’ from massive clusters

(Banerjee, Kroupa & Oh 2012; Lucas et al. 2018). Although diffuse or ‘leaky’ clusters (Pfalzner 2009) have sizes of about an order-of-magnitude larger than compact clusters (e.g. Cyg OB2), they can be thought of as assemblies of compact clusters, given that they have substantial substructures (Wright et al. 2014). Finally, if the initial cluster is small enough, it can be dissolved (or nearly dissolved) due to gas dispersion and mass-loss during SNe (Brinkmann et al. 2017, Shukirgaliyev et al. 2017).

Observations therefore indicate that all OB stars, including the progenitor isolated SNRs, can be considered to have formed in massive compact clusters.

## 5.2 Number statistics of SNe and massive clusters

Based on above discussions, we can therefore argue that the massive progenitors of apparently isolated SNRs can be considered as belonging to clusters in which the number of massive (OB) stars is  $\lesssim 2$ . The cluster luminosity function (Williams & McKee 1997) is observed to be  $dN/dN_{\text{OB}} \propto N_{\text{OB}}^{-2}$ , where  $N_{\text{OB}}$  is the number of OB stars in a cluster. This implies that roughly half the clusters would produce an apparently isolated (core collapse) SNR, since (for a lower limit of a massive star cluster being that with a single OB star)

$$\frac{\int_1^2 N_{\text{OB}}^{-2} dN_{\text{OB}}}{\int_1^{\infty} N_{\text{OB}}^{-2} dN_{\text{OB}}} \approx \frac{1}{2} \quad (12)$$

which is almost independent of the upper limit of total number of OB stars in a clusters which is roughly  $\sim 7000$  (McKee & Williams 1997).

In comparison,  $\gamma$ -ray bright clusters ( $\gamma$ -ray luminosity  $\gtrsim 10^{35} \text{ erg s}^{-1}$ ) have typically  $\sim 50$ – $100$  OB stars (Gupta et al. 2018b). This mass function implies a ratio of core-collapse SNRs to WTS gamma-ray sources is

$$\frac{\int_1^2 N_{\text{OB}}^{-2} dN_{\text{OB}}}{\int_{50-100} N_{\text{OB}}^{-2} dN_{\text{OB}}} \approx \frac{1}{2} (50-100) = (25-50). \quad (13)$$

Observations show that in Sbc galaxies (Milky-Way-type) the ratio of thermonuclear to core-collapse SNe is  $\sim 1/3$  (Mannucci et al. 2005). Adding thermonuclear SNRs, this indicates a ratio of SNRs to WTS  $\gamma$ -ray sources in our Galaxy of order 33–65.

We can check this argument by counting the SNRs and  $\gamma$ -ray bright clusters in a given volume. The size of the sampling volume is hard to decide, since  $\gamma$ -ray bright clusters are rare: there are only three  $\gamma$ -ray bright clusters near us, Cygnus at  $\approx 1.4$  kpc, Westerlund 1 at  $\approx 4$  kpc (Aharonian, Yang & de Oña Wilhelmi 2019), and Westerlund 2 at  $\approx 5$  kpc (Yang et al. 2018). Therefore, it makes sense to use all these three and use a sphere of radius 5 kpc around us. Counting the number of SNRs from the available catalogue, we find 124 of them within a distance of 5 kpc (listed in Table C1 of Appendix C), so that the ratio 124: 3 falls in the ballpark of the above estimate.

This match can be regarded as a consistency check for our proposed scenario, and this implies that isolated SNRs can indeed be considered as part of the phenomena of star clusters. Therefore, the two types of CR acceleration sites can indeed be put on a common platform.

## 5.3 Contributions of WTS and SN shocks in total energy budget of GCRs

The next issue to consider is the energy budget of GCRs from these two sites. It can be shown that these two classes of sources are

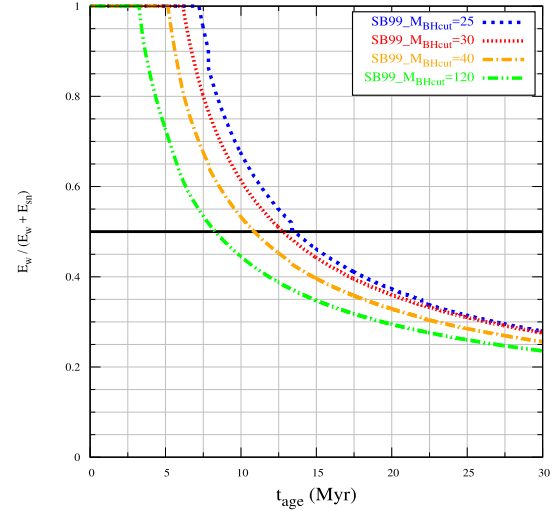


**Figure 16.** Contribution to stellar winds in the total mechanical energy output of a typical star cluster until a given epoch. All curves are obtained using the STARBURST99 stellar synthesis code (Leitherer et al. 1999) for the Kroupa initial mass function (Kroupa 2002). Each curve represents a model with different black hole mass,  $M_{\text{BHcut}}$  (blue –  $25 M_{\odot}$ , red –  $30 M_{\odot}$ , yellow –  $40 M_{\odot}$ , and green –  $120 M_{\odot}$ ). The figure shows that wind mechanical energy dominates over SN energy before  $\gtrsim 11 \pm 3$  Myr.

energetically comparable (as pointed out in 1980s, see e.g. Abbott, Biegging & Churchwell 1981), WTS being dominant in young phase of clusters. Fig. 16 plots the evolution of the contribution of stellar winds to the total mechanical energy of a star cluster, using STARBURST99 (Leitherer et al. 1999), and Kroupa initial mass function (Kroupa 2002), for different assumptions of black hole mass cut-off. The curves in the figure show that the fraction of the total shock energy in WTS for a massive cluster is always  $\geq 0.25$ , and is larger than 0.5 for clusters younger than  $\approx 10$  Myr, thereafter decreasing with time because of the increasing number of SNe. Therefore, *at least a quarter, if not a larger fraction, of the GCRs can be ascribed to WTSs in star clusters.*

For typical parameters, the average mechanical power in stellar winds within the solar circle (Reed 2005) is  $L_w \sim 10^{36} \text{ erg s}^{-1} N_{\text{OB}} \approx 2 \times 10^{41} \text{ erg s}^{-1}$  consistent with recent estimates (Seo, Kang & Ryu 2018). If this represents a quarter of the total mechanical energy in SNS and WTS, then this implies a mechanical energy budget for SNSs of  $6 \times 10^{41} \text{ erg s}^{-1}$ , which in turn corresponds to an SN rate of  $\sim 2$  per century, consistent with the observed rate of 2 per century (Diehl et al. 2006). Incidentally, with a typical efficiency of CR acceleration  $\sim 0.1$ , the total mechanical luminosity of  $8 \times 10^{41} \text{ erg s}^{-1}$  is comparable to the inferred GCR luminosity (Strong et al. 2010) of  $\sim 8 \times 10^{40} \text{ erg s}^{-1}$ .

Therefore, the scenario of CR acceleration in WTS and SNSs is consistent with respect to the energy budget.

## 5.4 Maximum energy of CRs

The importance of WTS as CR sources becomes crucial at high energies (Cesarsky & Montmerle 1983), since the observed  $\gamma$ -ray spectra of clusters are flatter than that of SNRs (Aharonian et al. 2019). The maximum CR energy depends on the extent of the accelerating region, in this case, the width of the shocked wind region, which separates the CD and WTS. The distance of the WTS

is roughly given by

$$R_{\text{ts}} \approx 25 \text{ pc } n_1^{-3/10} \dot{M}_{-4}^{1/2} L_{w,38}^{-1/5} v_{w,2000}^{1/2} t_{3M}^{2/5}, \quad (14)$$

where  $n_1$  is the ambient particle density in units of  $10 \text{ cm}^{-3}$ ,  $\dot{M}_{-4}$  is mass-loss rate in units of  $10^{-4} M_{\odot} \text{ yr}^{-1}$ ,  $v_{w,2000}$  is wind speed in units of  $2000 \text{ km s}^{-1}$ ,  $L_{w,38}$  is wind mechanical power in units of  $10^{38} \text{ erg s}^{-1}$ ,  $t_{3M}$  is time in 3 Myr unit. The distance of the CD is  $(\eta L_w t^3 / \rho)^{1/5}$ , where  $\eta \sim 0.2$  takes into account energy lost in radiative cooling (Sharma et al. 2014). For the same fiducial parameters, this distance is given by  $\sim 62 \text{ pc}$ . Therefore, for a  $10^4 M_{\odot}$  cluster, the extent of the shocked wind region at  $\sim 3 \text{ Myr}$  (when WTS dominates) is  $\sim 40 \text{ pc}$ . This estimate is also borne out with our 1D simulation (see e.g. Fig. 3 for compact star clusters).

According to the Hillas criterion (Hillas 1984), the accelerating region should be larger than  $2r_L/\beta$  where  $r_L$  is the Larmor radius of a particle, which leads to a maximum energy

$$E \leq \frac{1}{2} 10^{15} \text{ eV } L_{\text{pc}} B_{\mu\text{G}} Z \beta, \quad (15)$$

where  $\beta$  is the ratio of shock speed to that of light, and  $L_{\text{pc}}$  is the extent of the accelerating region in parsec.<sup>4</sup> With a  $10 \mu\text{G}$  field, and wind velocity  $\sim 2000 \text{ km s}^{-1}$ , this implies a maximum energy (Hillas 1984) of  $\sim 1.5 Z \text{ PeV}$ , much larger than in isolated SNR.

The maximum energy of CRs in different acceleration sites has long been a debatable issue. Although it is believed that SNRs likely accelerate to at the most PeV energy (Hillas 2005; Bell 2013; Amato 2014), Ptuskin, Zirakashvili & Seo (2010) have argued that Type IIb SNe, a rare subclass, comprising  $\sim 3$  per cent of core-collapse SNe, may accelerate up to 100 PeV at early stages of evolution. In the context of SNe shocks in stellar wind, Völk & Biermann (1988) had argued that SNe shocks expanding in a wind bubble could circumvent the problems with isolated SNRs, while Bykov (2014) has discussed the possibility of accelerating CRs (protons) to tens of PeV in the colliding shocks (SNe shock and WTS), which would enable Fermi first-order acceleration. Our inference above is qualitatively different from these models in the sense that it is independent of SNe event in a star cluster.

We also note that LOFAR observations show PeV CRs to be enriched in low- $Z$  nuclei (Buitink et al. 2016), consistent with their being accelerated from CNO enriched wind material in SBs (Thoudam et al. 2016). It is also possible that the hard component of CRs due to WTS is the one inferred to be present in molecular clouds (de Boer et al. 2017). Therefore, WTSs are potential PeVatrons and they should be studied in detail in this regard.

### 5.5 Decoupling of grammage from ISM

Our proposed scenario can also provide the astrophysical framework for the phenomenologically motivated models of CR propagation in which the grammage traversed by CRs are mostly near the source (Blasi & Serpico 2009; Cowsik & Madziwa-Nussinov 2016; Eichler 2017; Biermann et al. 2018). In these models, the diffusion property of CR particles is assumed to be different inside the ‘cocoon’ surrounding the CR acceleration sites than elsewhere in the ISM in order to alleviate problems associated with secondary production.

The scenario of CR acceleration in SBs satisfies the basic premises of these models, since most of the CR collisions occur in the outer shell of shocked ISM, whereas CRs are advected by

the wind in the inner regions. The grammage suffered by CRs in the shocked ISM region is  $\sim 10 \text{ g cm}^{-2}$ , comparable to the total grammage of GCR (Gabici et al. 2019), since the typical residence time is  $t_r \sim 1 \text{ Myr}$  ( $\sim \kappa/v^2$ , for a diffusion coefficient  $\kappa \sim 10^{27} \text{ cm}^2 \text{ s}^{-1}$  and  $v \sim 50 \text{ km s}^{-1}$ , the typical outer shock speed), and typical density in this region is  $\sim 10 \text{ cm}^{-3}$ .

Therefore, CR grammage can be decoupled from Galactic residence time, alleviating a number of outstanding problems (Butt 2009; Gabici et al. 2019). Instead of listing them all, we mention one of the problems here, that of the observed scaling of light elements with metallicity in halo stars (Parizot & Drury 1999). In the case of isolated SNRs (which accelerates ISM particles), the Li/Be/B abundance is expected to scale as  $Z^2$ , since both CR and the target gas share the same metallicity. In the case of WTS, the metallicity of CRs is independent of that of the ambient ISM, the abundance of spallation products should scale as  $Z$ , as observed (Parizot & Drury 1999).

### 5.6 Caveats and future directions

In this study, we show the first calculations for estimating the energetics of the wind and SN shocks in isolated stars/star clusters. We have used a shock detection algorithm and three different tracers to quantify the fraction of shock energy processed by wind, SN ejecta, and ambient material. Although in the above sections, we have shown that this study has succeeded in revealing answers to various problems in GCRs, below we highlight some of the limitations of our models and future directions.

(i) **Non-radiative strong shocks:** We have considered the Rankine–Hugoniot shock jump condition to find the upstream Mach number ( $M_1$ ) (see step 4 in Section 3.1), which has been used for a robust estimation of mass and energy fluxes. However, it is worth mentioning that this assumption may not be suitable for all types of shocks. For example, in the case of radiative shocks, the compression ratio  $\propto M_1^2$  and the ratio of upstream to downstream pressures does not follow the Rankine–Hugoniot conditions (see e.g. Shu 1991). Therefore, by choosing the Rankine–Hugoniot shock jump conditions, we restrict the applicability of analysis for non-radiative and high Mach number shocks. This assumption is presently reasonable because CR acceleration efficiency in radiative shocks is still not clearly understood.

(ii) **Spherical shocks and mixing:** Due to the assumed 1D spherical geometry in our hydro simulations, all shock surfaces are considered spherical. Some studies have shown that spherical symmetry breaks when two shocks collide (see e.g. Section 4.2 in Dwarkadas 2007b). Inside a hot bubble (especially at the CD), various instabilities (such as Vishniac instability and thermal instability) can fragment shock surfaces, which can allow mixing between different material. Multidimensional analysis is required to address this.

(iii) **Wind structure:** We have assumed that wind luminosity and the mass-loss rate of individual stars are constant until the SN epoch. In a realistic scenario, wind evolves with time. In Appendix B, we have shown one such example and confirm that the results are consistent with our prediction. For a better understanding, it will be good to confirm it for stars with different masses. These investigations demand the information related to the stellar evolution of each star, which currently does not have a unique answer because of its dependences on various parameters (e.g. metallicity, stellar rotation, and evolutionary tracks). We expect that in massive clusters, the details of individual stars will not affect

<sup>4</sup>Biermann et al. (2018) argued that the ‘ $\beta$ ’ term in equation (15) may be absent, depending on the magnetic field configuration, see e.g. Jokipii (1987)

the qualitative results of this paper. This can be investigated in the future.

## 6 CONCLUSIONS

With 1D numerical hydrodynamical simulation of stellar winds in star clusters, we have studied the relative importance of SNe shocks and WTSs in clusters, both compact and massive, and also in the case of SNe shocks running into stellar winds of the progenitor star. Our findings are as follows:

(i) WTSs process more than 1/4 of the total mechanical power in a star cluster, and this fraction rises to  $\geq 0.5$  for young ( $\leq 10$  Myr) clusters (Fig. 16). Therefore, a significant fraction of GCRs are accelerated in these shocks in massive compact star clusters.

(ii) A large fraction ( $\approx 2/3$ – $6/7$ ) of the total energy processed by WTS and SNe shocks goes to accelerate the stellar wind material, enriched in  $^{22}\text{Ne}$  (Fig. 12). Using this ratio as an energy weightage for the stellar wind and SN ejecta, we show that the time-averaged ratio of  $^{22}\text{Ne}/^{20}\text{Ne}$  matches the observed value.

(iii) We also show that the scenario often quoted in literature for explaining the Neon ratio, namely, by SNe shocks in a stellar wind of progenitor star, is problematic because we find that the reverse shock in this case is as efficient as the forward shock, and it would accelerate SN ejecta (rich in  $^{20}\text{Ne}$ ) posing a problem for the isotope ratio.

(iv) The combined effect of WTSs and SNe shocks in star clusters can explain the observed Neon isotope ratio (Fig. 15), unlike previous approaches of either SNe shocks (in stellar winds) or only stellar winds (e.g. Binns et al. 2008).

(v) We take this approach forward to suggest that these two sources can be brought under a same umbrella of CR acceleration in SBs, since SNe and stellar wind are both related to massive stars and they form in clusters. Isolated SNRs can be considered as representing the lower end of the star cluster mass function.

(vi) Using the luminosity function of OB associations, we show that the expected ratio of isolated SNRs to  $\gamma$ -ray bright star clusters matches observed numbers (Section 5.2).

(vii) We argue that the accelerating region in the case of WTSs is large enough to explain CRs in PeV range (Section 5.4), thus making WTSs an important complementary source of CRs.

(viii) The fact that most of the CR interactions occur in the SB, with a grammage that corresponds to the observed grammage of GCRs (Section 5.5), decouples the CR grammage from the Galactic residence time and helps solve other long-standing problems with the standard paradigm of SNRs as CR acceleration sites.

The integrated picture of CR acceleration in SBs inflated by clustered WTS and SN presented here can solve these problems as well as explain  $^{22}\text{Ne}/^{20}\text{Ne}$  ratio, while being consistent with the number statistics of SNRs and WTS sources.

## ACKNOWLEDGEMENTS

We thank S. Banerjee, P. L. Biermann, P. Chandra, and N. Prantzos for useful discussions. PS thanks the Humboldt Foundation for supporting his sabbatical at MPA. PS acknowledges the Department of Science and Technology for a Swarnajayanti Fellowship (DST/SJF/PSA-03/2016-17). SG thanks CSIR India for the SPM Fellowship. We thank the anonymous referee for insightful comments on the manuscript of this paper.

## REFERENCES

- Abbott D. C., Biegging J. H., Churchwell E., 1981, *ApJ*, 250, 645  
 Ackermann M. et al., 2011, *Science*, 334, 1103  
 Aharonian F., Yang R., de Oña Wilhelmi E., 2019, *Nat. Astron.*, 3, 561  
 Amato E., 2014, *Int. J. Mod. Phys. D*, 23, 1430013  
 Banerjee S., Kroupa P., Oh S., 2012, *ApJ*, 746, 15  
 Bell A. R., 2013, *Astropart. Phys.*, 43, 56  
 Biermann P. L., Cassinelli J. P., 1993, *A&A*, 277, 691  
 Biermann P. L. et al., 2018, *Adv. Space Res.*, 62, 2773  
 Binns W. R. et al., 2008, *New Astron. Rev.*, 52, 427  
 Blasi P., Serpico P. D., 2009, *Phys. Rev. Lett.*, 103, 081103  
 Brinkmann N., Banerjee S., Motwani B., Kroupa P., 2017, *A&A*, 600, A49  
 Buitink S. et al., 2016, *Nature*, 531, 70  
 Butt Y., 2009, *Nature*, 460, 701  
 Bykov A. M., 2014, *A&AR*, 22, 77  
 Cesarsky C. J., Montmerle T., 1983, *Space Sci. Rev.*, 36, 173  
 Chevalier R. A., Clegg A. W., 1985, *Nature*, 317, 44  
 Cowsik R., Madziwa-Nussinov T., 2016, *ApJ*, 827, 119  
 de Boer W., Bosse L., Gebauer I., Neumann A., Biermann P. L., 2017, *Phys. Rev. D*, 96, 043012  
 Dermer C. D., Powale G., 2013, *A&A*, 553, A34  
 Diehl R. et al., 2006, *Nature*, 439, 45  
 Dwarkadas V. V., 2007a, *Ap&SS*, 307, 153  
 Dwarkadas V. V., 2007b, *ApJ*, 667, 226  
 Eichler D., 2017, *ApJ*, 842, 50  
 Gabici S., Evoli C., Gaggero D., Lipari P., Mertsch P., Orlando E., Strong A., Vittino A., 2019, *Int. J. Mod. Phys. D*, 28, 1930022–339  
 Grenier I. A., Black J. H., Strong A. W., 2015, *ARA&A*, 53, 199  
 Gupta S., Nath B. B., Sharma P., Eichler D., 2018a, *MNRAS*, 473, 1537  
 Gupta S., Nath B. B., Sharma P., 2018b, *MNRAS*, 479, 5220  
 Higdon J. C., Lingenfelter R. E., 2003, *ApJ*, 590, 822  
 Hillas A. M., 1984, *ARA&A*, 22, 425  
 Hillas A. M., 2005, *J. Phys. G: Nucl. Phys.*, 31, R95  
 Jokipii J. R., 1987, *ApJ*, 313, 842  
 Kalyashova M. E., Bykov A. M., Osipov S. M., Ellison D. C., Badmaev D. V., 2019, *J. Phys. Conf. Ser.*, 1400, 22011  
 Kroupa P., 2002, *Science*, 295, 82  
 Leitherer C. et al., 1999, *ApJS*, 123, 3  
 Limongi M., Chieffi A., 2018, *ApJS*, 237, 13  
 Lopez L. A., Krumholz M. R., Bolatto A. D., Prochaska J. X., Ramirez-Ruiz E., Castro D., 2014, *ApJ*, 795, 121  
 Lucas W. E., Rybak M., Bonnell I. A., Gieles M., 2018, *MNRAS*, 474, 3582  
 Maeder A., Meynet G., 1993, *A&A*, 278, 406  
 Mannucci F., Della Valle M., Panagia N., Cappellaro E., Cresci G., Maiolino R., Petrosian A., Turatto M., 2005, *A&A*, 433, 807  
 McKee C. F., Williams J. P., 1997, *ApJ*, 476, 144  
 Mewaldt R. A., 1981, in Ryter C., ed., *International Cosmic Ray Conference*, D. Reidel, Dordrecht, Holland, p. 49  
 Mignone A., Bodo G., Massaglia S., Matsakos T., Tesileanu O., Zanni C., Ferrari A., 2007, *ApJS*, 170, 228  
 Murphy R. P. et al., 2016, *ApJ*, 831, 148  
 Parizot E., Drury L., 1999, *A&A*, 349, 673  
 Pflanzner S., 2009, *A&A*, 498, L37  
 Portegies Zwart S. F., McMillan S. L. W., Gieles M., 2010, *ARA&A*, 48, 431  
 Prantzos N., 2012, *A&A*, 538, A80  
 Ptuskin V., Zirakashvili V., Seo E.-S., 2010, *ApJ*, 718, 31  
 Reed B. C., 2005, *AJ*, 130, 1652  
 Sana H., 2013, in Pavlovski K., Tkachenko A., Torres G., eds, *EAS Publ. Ser. Vol. 64, Setting a New Standard in the Analysis of Binary Stars*. Cambridge Univ. Press, Cambridge, p. 147  
 Seo J., Kang H., Ryu D., 2018, *J. Korean Astron. Soc.*, 51, 37  
 Sharma P., Roy A., Nath B. B., Shchekinov Y., 2014, *MNRAS*, 443, 3463  
 Shukirgaliyev B., Parmentier G., Berczik P., Just A., 2017, *A&A*, 605, A119  
 Shu F. H., 1991, *The Physics of Astrophysics: Volume II: Gas Dynamics*, University Science Books, USA

- Strong A. W., Porter T. A., Digel S. W., Jóhannesson G., Martin P., Moskalenko I. V., Murphy E. J., Orlando E., 2010, *ApJ*, 722, L58
- Sutherland R. S., Dopita M. A., 1993, *ApJS*, 88, 253
- Tezhinsky I., Dwarkadas V. V., Pohl M., 2013, *A&A*, 552, A102
- Thoudam S., Rachen J. P., van Vliet A., Achterberg A., Buitink S., Falcke H., Hörand el J. R., 2016, *A&A*, 595, A33
- Truelove J. K., McKee C. F., 1999, *ApJS*, 120, 299
- Völk H. J., Biermann P. L., 1988, *ApJ*, 333, L65
- Weaver R., McCray R., Castor J., Shapiro P., Moore R., 1977, *ApJ*, 218, 377
- Wiedenbeck M. E. et al., 1999, *ApJ*, 523, L61
- Wiedenbeck M. E., Greiner D. E., 1981, *Phys. Rev. Lett.*, 46, 682
- Williams J. P., McKee C. F., 1997, *ApJ*, 476, 166
- Wright N. J., Parker R. J., Goodwin S. P., Drake J. J., 2014, *MNRAS*, 438, 639
- Yang R.-z., de Oña Wilhelmi E., Aharonian F., 2018, *A&A*, 611, A77

## APPENDIX A: 3D SET-UP

Here, we present the set-up of our 3D simulations discussed in Section 2.1. We simulate two star clusters with two different core radii  $R_c$ . Both clusters have 12 massive stars (i.e.  $N_{\text{OB}} = 12$ ), which corresponds to a cluster of stellar mass  $10^3 M_{\odot}$  (for a standard Kroupa initial mass function with lower and upper cut-off masses 0.1 and  $120 M_{\odot}$ ; Kroupa 2002). We have solved the standard Euler equations in 3D Cartesian geometry using the PLUTO code (Mignone et al. 2007), where the HLLC Riemann solver is used (CFL number 0.3) and the computational box extends from  $-60$  pc to  $+60$  pc along  $x$ ,  $y$ , and  $z$  directions. At  $t = 0$ , we assume that ambient density is uniform with  $\rho = 50 m_{\text{H}} \text{cm}^{-3}$ , and pressure is  $10^{-12} \text{dyn cm}^{-2}$ . Radiative cooling has been included both runs. Locations of the stars are randomly chosen by using a Gaussian random number generator, where we have used two sets of mean deviations,  $\sigma_{x,y,z} = 0.5$  pc and  $\sigma_{x,y,z} = 5$  pc, to represent compact and loosely bound star clusters, respectively. For each star, we have assumed  $\dot{M} = 8 \times 10^{-7} M_{\odot} \text{yr}^{-1}$  and  $L_w = 10^{36} \text{erg s}^{-1}$ , which are injected in small spherical regions of radius  $\delta r_{\text{inj}} = 0.2$  pc (for details see section 4.2 in Gupta et al. 2018b).

## APPENDIX B: TIME-DEPENDENT LUMINOSITY MODEL

To estimate the fraction of shock energy encountered by wind material and SNe ejecta, in the previous sections, we have considered a time-independent wind model, where it has been assumed the wind mechanical luminosity of each star in a cluster is  $10^{36} \text{erg s}^{-1}$  until it explodes as SN. Here, we investigate the effect of the time-dependent wind luminosity in our calculation.

### B1 Single star

To begin with, we first investigate the Case II by considering a time-dependent wind luminosity and mass-loss rate. We make use of figs 1 and 2 of Dwarkadas (2007b) to calculate the wind luminosity profile for a  $35 M_{\odot}$  star, which is shown in the left-hand panel of Fig. B1. A  $35 M_{\odot}$  star has three distinct evolution phases: (i) main sequence (until  $\approx 4.6$  Myr), (ii) red-supergiant phase (duration  $\approx 0.2$  Myr), and (iii) Wolf–Rayet (WR) phase ( $\approx 0.2$  Myr). At the end of the WR phase, the star explodes. The mass and energy ejected at the SN explosion is taken as  $7.75 M_{\odot}$  (as in Dwarkadas 2007b) and  $10^{51} \text{erg}$ , respectively. We use all this information to set up our simulation.

We investigate the interaction of SN shock with a wind-driven bubble of  $35 M_{\odot}$  star and find that the structure is similar to Dwarkadas (2007b). In the right-hand panel of Fig. B1, we present the shock energetics for wind, SN ejecta, and ambient material, as shown previously (e.g. Fig. 7). The figure shows that before SN explosion (i.e.  $t_{\text{dyn}} < 5$  Myr), shock energy is mainly processed by wind material (green curve). After 5 Myr, the red curve appears (representing the acceleration of SN ejecta). Then, the green and red curves become comparable, i.e. shock energy encountered by SN ejecta is comparable to that by the wind. Therefore, the acceleration of SN ejecta cannot be ignored in this scenario, which confirms our prediction of Section 4.1.2.

### B2 Star cluster

We use a stellar synthesis code STARBURST99 (Leitherer et al. 1999) to obtain the time evolution of wind luminosity, stellar mass-loss

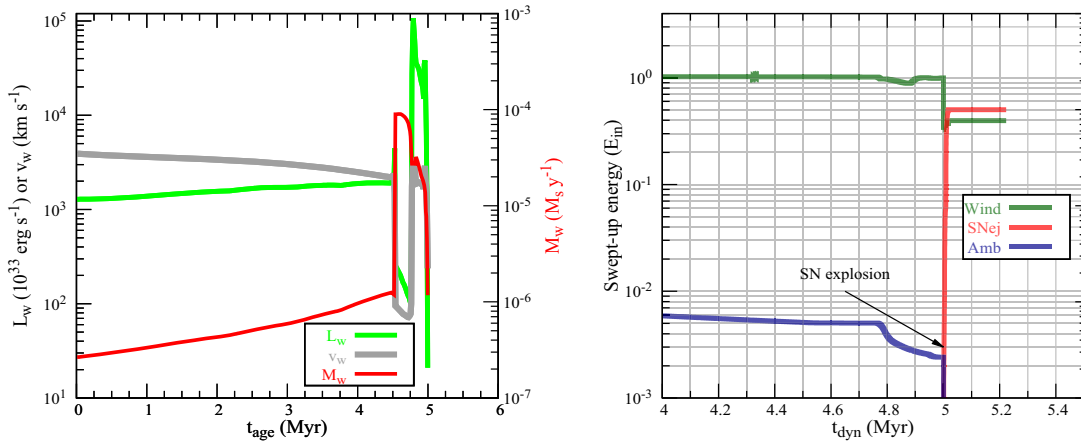


**Figure B1.** Case II (SN in wind of progenitor star) with time-dependent wind luminosity. The left-hand panel displays stellar wind luminosity (green), wind velocity (grey), and mass-loss rate (red) of a  $35 M_{\odot}$  star. The right-hand panel represents the shock energy processed by stellar wind (green), SN ejecta (red), and ambient material (blue), similar to the bottom right panel of Fig. 7. Shock energy encountered by ambient material is sub-dominated compared to wind and SN ejecta because outer shock becomes weak due to radiative energy losses, as seen previously. The figure shows that the shock energy processed by wind material is comparable to SN ejecta, which confirms our conclusion of Section 4.1.2.

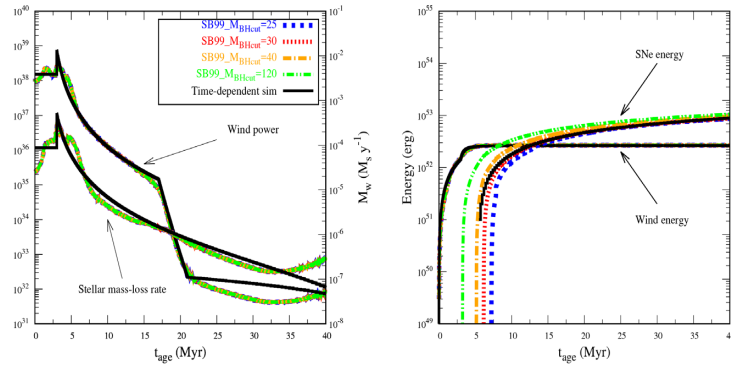


**Figure B2.** Time-dependent wind model. (Left-hand panel) Time evolution of stellar wind luminosity and mass-loss rate of a cluster of mass  $10^4 M_{\odot}$  obtained using the STARBURST99 stellar synthesis code (Leitherer et al. 1999). Each curve represents a model with different black hole cut-off mass,  $M_{\text{BHcut}}$  (blue –  $25 M_{\odot}$ , red –  $30 M_{\odot}$ , yellow –  $40 M_{\odot}$ , and green –  $120 M_{\odot}$ ). The figure shows that stellar wind luminosity decreases and becomes almost negligible after  $\gtrsim 15$  Myr. (Right-hand panel) Comparison between wind mechanical energy and SN energy in a cluster. The different colours show that the time when SN energy dominates over wind energy depends on  $M_{\text{BHcut}}$  and it occurs after  $\approx 11 \pm 3$  Myr. In both panels, the black curves represent an injection model used to show the effect of time-dependent wind model in our calculation.

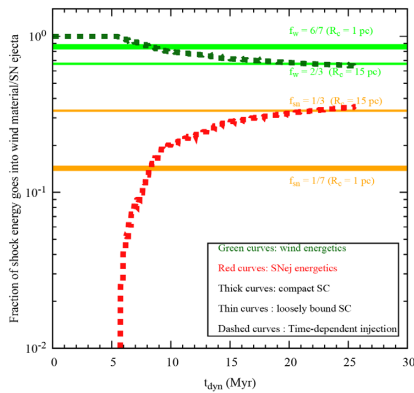


**Figure B3.** Shock energetics of wind material (green) and SN ejecta (red) for a time-dependent wind model (also see Fig. 12). The dashed curves represent a time-dependent wind model for a compact star cluster where mass and energy have been injected according to the black curves in Fig. B2. These curves confirm that the shock energy encountered by wind material is larger than that by SN ejecta.

rate, and SNe energy of a cluster of mass  $10^4 M_{\odot}$  for four different black hole cut-off masses: 25, 30, 40, and  $120 M_{\odot}$ . The wind mechanical power and mass-loss rates are shown in the left-hand panel of Fig. B2. The figure shows that the wind mechanical power and mass-loss rates do not depend on the black hole cut-off mass, as expected. The right-hand panel shows the total energy deposited by SNe and by winds in the cluster until a given epoch. The black curves represent fitted curves used in our model to inject stellar wind and SN energy. The fraction of shock energy processed in wind material and SNe ejecta are shown in Fig. B3. The figure shows that the fraction of shock energy processed in wind is larger than that in SN ejecta.

### APPENDIX C: SNRS

Table C1 shows a list of 124 SNRs that have been used in Section 5.2 to discuss number statistics of SNe and massive clusters.

**Table C1.** This table provides a list of SNRs which are located within 5 kpc. [1] and [2] refer to [1] <https://arxiv.org/abs/1409.0637>; <https://www.mrao.ac.uk/surveys/snrs/> and [2] [https://hea-www.cfa.harvard.edu/ChandraSNR/snrcat\\_gal.html](https://hea-www.cfa.harvard.edu/ChandraSNR/snrcat_gal.html).

	Galactic coordinates ( $l, b$ )	Distance (kpc)	Ref.
1.	4.5, + 6.8	3.3–5.1	[1]
2.	5.2, – 2.6	4.3–5.2	[1]
3.	5.7, – 0.1	2.9–3.2	[2]
4.	6.4, – 0.1	2.2	[1]
5.	7.7, – 3.7	3.2–6	[1]
6.	8.7, – 0.1	4.0	[1]
7.	11.0, – 0.0	5.0	[1]
8.	11.1, + 0.1	4.4	[1]
9.	13.3, – 1.3	2–4	[1]
10.	5.7, – 0.1	3.2	[1]
11.	7.5, – 1.7	1.7–2.0	[2]
12.	15.1, – 1.6	2.1	[1]
13.	15.4, + 0.1	4.8	[1]
14.	18.6, – 0.2	4.2–4.6	[1]
15.	18.9, – 1.1	4.2–4.6	[1]
16.	19.1, + 0.2	1–2	[1]
17.	21.5, – 0.9	4.7	[1]
18.	22.7, – 0.2	4.5–4.9	[1]
19.	23.3, – 0.3	4.6–5.0	[1]
20.	24.7, – 0.6	–4	[1]
21.	24.7, + 0.6	2–3.7	[1]
22.	28.8, + 1.5	3.8–4.0	[1]
23.	29.6, + 0.1	4.4–5.0	[1]
24.	29.7, – 0.3	5.0	[1]
25.	32.0, – 4.9	1.8	[1]
26.	32.1, – 0.9	4.6	[1]
27.	32.8, – 0.1	4.5–5.1	[1]
28.	34.7, – 0.4	2.1–3	[1]
29.	40.5, – 0.5	3.2	[1]
30.	42.0, – 0.1	3.1–3.9	[1]
31.	49.2, – 0.7	4.3	[1]

Table C1 – continued

	Galactic coordinates ( $l, b$ )	Distance (kpc)	Ref.
32.	53.6, – 2.2	2.8	[1]
33.	55.7, + 3.4	0.56	[1]
34.	57.2, + 0.8	3.5	[1]
35.	21.5, – 0.9	4.7	[2]
36.	21.9, – 0.1	4.3	[2]
37.	23.5, + 0.1	5	[2]
38.	26.6, – 0.51	1.3	[1]
39.	34.0, + 20.3	1.4	[1]
40.	59.2, – 0.47	2.5	[1]
41.	65.3, + 5.7	0.8	[1]
42.	65.7, + 1.2	1.5	[1]
43.	65.8, – 0.5	1.9–2.7	[1]
44.	66.0, – 0.0	2.0–2.6	[1]
45.	67.6, + 0.9	1.8–2.2	[1]
46.	70.0, – 21.5	$\lesssim 3$	[1]
47.	73.9, + 0.9	0.5–4.0	[1]
48.	74.0, – 8.5	0.44	[1]
49.	78.2, + 2.1	1.7–2.6	[1]
50.	82.2, + 5.3	1.3–3.2	[1]
51.	85.4, + 0.7	3.5	[1]
52.	85.9, – 0.6	4.8	[1]
53.	89.0, + 4.7	0.8	[1]
54.	93.3, + 6.9	2.2	[1]
55.	93.7, – 0.2	1.5	[1]
56.	10.9, – 45.4	0.25	[2]
57.	25.1, – 2.3	2.9	[1]
58.	33.6, + 0.1	3.5–7.1	[1]
59.	39.7, – 2.0	3.5–6.5	[1]
60.	42.8, + 0.6	2.8–7.7	[1]
61.	69.0, + 2.7	1.5	[1]
62.	106.3, + 2.7	0.8–3.0	[1]
63.	126.2, + 1.6	4.5	[1]
64.	152.4, – 2.1	1	[1]
65.	284.3, – 1.8	2.9	[1]
66.	299.2, – 2.9	5	[1]
67.	96.0, + 2.0	4	[1]
68.	108.2, – 0.6	3.2	[1]
69.	109.1, – 1.0	3.2	[1]
70.	111.7, – 2.1	3.3–3.7	[1]
71.	113.0, + 0.2	3.1	[1]
72.	114.3, + 0.3	0.7	[1]
73.	116.5, + 1.1	1.6	[1]
74.	116.9, + 0.2	1.6	[1]
75.	119.5, + 10.2	1.4	[1]
76.	120.1, + 1.4	2.4	[1]
77.	127.1, + 0.5	1.2–1.3	[1]
78.	130.7, + 3.1	2	[1]
79.	132.7, + 1.3	2	[1]
80.	156.2, + 5.7	1.7	[1]

Table C1 – continued

	Galactic coordinates ( $l, b$ )	Distance (kpc)	Ref.
81.	160.9, + 2.6	<4	[1]
82.	166.0, + 4.3	4.5	[1]
83.	178.2, – 4.2	2.9	[1]
84.	180.0, – 1.7	0.36–0.88	[1]
85.	184.6, – 5.8	2	[1]
86.	189.1, + 3.0	1.5–2.0	[1]
87.	190.9, – 2.2	1.0	[1]
88.	205.5, + 0.5	1.6	[1]
89.	206.9, + 2.3	2.2	[1]
90.	260.4, – 3.4	2.2	[1]
91.	261.9, + 5.5	2.9	[1]
92.	263.9, – 3.3	0.25	[1]
93.	266.2, – 1.2	<1	[1]
94.	80.2, – 1.0	1.5	[2]
95.	107.5, – 1.5	1.1	[2]
96.	162.8, – 16.0	0.5	[2]
97.	276.5, + 19.0	0.06–0.3	[2]
98.	287.4, – 0.6	3	[1]
99.	296.5, + 10.0	1.3–3.9	[1]
100.	308.8, – 0.1	2	[1]
101.	309.8, + 0.0	5	[1]
102.	315.4, – 2.3	2.3	[1]
103.	317.3, – 0.2	4.0	[1]
104.	326.3, – 1.8	3.4–5.8	[1]
105.	327.4, + 0.4	4.3–5.4	[1]
106.	327.6, + 14.6	2.2	[1]
107.	330.0, + 15.0	0.15–0.5	[1]
108.	332.4, – 0.4	3.1	[1]
109.	332.5, – 5.6	3.0	[1]
110.	337.3, + 1.0	5	[1]
111.	319.9, – 0.7	2.5	[2]
112.	323.9, – 0.00	3.1	[2]
113.	343.0, – 6.0	1.5	[1]
114.	347.3, – 0.5	1.3	[1]
115.	350.1, – 0.3	4.5	[1]
116.	355.6, – 0.0	3	[1]
117.	359.1, – 0.5	5	[1]
118.	348.9, 0.4	3.6	[2]
119.	350.2, 0.8	0.27–0.39	[2]
120.	359.2, 0.8	5	[2]
120.	335.2, + 0.1	1.8	[1]
121.	336.7, + 0.5	3	[1]
122.	353.6, – 0.7	2.4–6.1	[1]
123.	343.1, – 0.7	2	[1]
124.	354.1, + 0.1	1.5	[1]

This paper has been typeset from a  $\text{\TeX}/\text{\LaTeX}$  file prepared by the author.